RESEARCH ARTICLE

Key Points:
- First lidar observations of repeated seasonal patterns of stratospheric gravity wave potential energy density and stability N^2 were made in Antarctica
- E_{pm} obey lognormal distributions, show more severe wave dissipation in winter, and the largest E_{pm} occurs when McMurdo is well inside polar vortex
- E_{pm} summer-winter asymmetry is mainly caused by critical level filtering, and wind speeds strongly affect the E_{pm} variations in winter

Correspondence to:
X. Chu and J. Zhao,
xinzhao.chu@colorado.edu;
jian.zhao@colorado.edu

Lidar Observations of Stratospheric Gravity Waves From 2011 to 2015 at McMurdo (77.84°S, 166.69°E), Antarctica: 2. Potential Energy Densities, Lognormal Distributions, and Seasonal Variations

Xinzhao Chu[1,2] (iD), **Jian Zhao**[1,2] (iD), **Xian Lu**[1,3] (iD), **V. Lynn Harvey**[4] (iD), **R. Michael Jones**[1] (iD), **Erich Becker**[5] (iD), **Cao Chen**[1,2] (iD), **Weichun Fong**[1,2] (iD), **Zhibin Yu**[1,2], **Brendan R. Roberts**[1,2], and **Andreas Dörnbrack**[6]

[1]Cooperative Institute for Research in Environmental Sciences, University of Colorado Boulder, Boulder, CO, USA, [2]Department of Aerospace Engineering Sciences, University of Colorado Boulder, Boulder, CO, USA, [3]Department of Physics and Astronomy, Clemson University, Clemson, SC, USA, [4]Laboratory for Atmospheric and Space Physics, University of Colorado Boulder, Boulder, CO, USA, [5]Leibniz Institute of Atmospheric Physics, University of Rostock, Kühlungsborn, Germany, [6]DLR Oberpfaffenhofen, Institute für Physik der Atmosphäre, Oberpfaffenhofen, Germany

Abstract Five years of Fe Boltzmann lidar's Rayleigh temperature data from 2011 to 2015 at McMurdo are used to characterize gravity wave potential energy mass density (E_{pm}), potential energy volume density (E_{pv}), vertical wave number spectra, and static stability N^2 in the stratosphere 30–50 km. E_{pm} (E_{pv}) profiles increase (decrease) with altitude, and the scale heights of E_{pv} indicate stronger wave dissipation in winter than in summer. Altitude mean $\overline{E}_{pm}$ and $\overline{E}_{pv}$ obey lognormal distributions and possess narrowly clustered small values in summer but widely spread large values in winter. $\overline{E}_{pm}$ and $\overline{E}_{pv}$ vary significantly from observation to observation but exhibit repeated seasonal patterns with summer minima and winter maxima. The winter maxima in 2012 and 2015 are higher than in other years, indicating interannual variations. Altitude mean $\overline{N^2}$ varies by ~30–40% from the midwinter maxima to minima around October and exhibits a nearly bimodal distribution. Monthly mean vertical wave number power spectral density for vertical wavelengths of 5–20 km increases from summer to winter. Using Modern Era Retrospective Analysis for Research and Applications version 2 data, we find that large values of $\overline{E}_{pm}$ during wintertime occur when McMurdo is well inside the polar vortex. Monthly mean $\overline{E}_{pm}$ are anticorrelated with wind rotation angles but positively correlated with wind speeds at 3 and 30 km. Corresponding correlation coefficients are −0.62, +0.87, and +0.80, respectively. Results indicate that the summer-winter asymmetry of $\overline{E}_{pm}$ is mainly caused by critical level filtering that dissipates most gravity waves in summer. $\overline{E}_{pm}$ variations in winter are mainly due to variations of gravity wave generation in the troposphere and stratosphere and Doppler shifting by the mean stratospheric winds.

Plain Language Summary Persistent and dominant inertia-gravity waves (IGWs) are meandering around McMurdo, Antarctica, from the stratosphere to the lower thermosphere all year round. However, the wave sources are still mysterious and in a hot debate. This paper represents a significant step forward in the wave source searching by the following intriguing findings: Large wave energy occurs when McMurdo is deep inside the polar vortex, consistent with the fact that the vertical propagation angle of McMurdo IGWs is shallow so that wave sources are not local; potential energy density shows the repeated seasonal patterns with summer minima and winter maxima, and larger energy density corresponds to strong surface and stratospheric winds, but minimal rotation angle of background winds. These findings imply that primary wave sources near the surface and secondary wave sources in the stratosphere could both exist, while background winds play a role of filtering certain wave spectra, Doppler-shifting vertical wavelengths, and therefore controlling wave propagation and dissipation. The complex interplay of wave source, dissipation, and saturation gives rise to what are observed in the current paper. These important observational facts help model simulations to narrow down the wave sources.

1. Introduction

The discovery of persistent gravity waves (with periods of 3–10 hr and vertical wavelengths of 20–30 km) in the mesosphere and lower thermosphere (MLT) by Fe Boltzmann lidar observations above McMurdo (77.83°S, 166.67°E), Antarctica, has posed intriguing questions and challenged the understanding of gravity

wave sources (Chen et al., 2016; Chen & Chu, 2017). No known sources could provide perpetual generation of gravity waves with such significant amplitudes (easily ±30 K around altitudes of 100 km), so various theories were invoked to attempt explanations. For example, Godin and Zabotin (2016) proposed resonant vibrations of the Ross Ice Shelf as a source of persistent gravity waves. In a case study, Chen et al. (2013) ray traced a 7.7-hr inertia-gravity wave (IGW) from the MLT above McMurdo to an unbalanced flow in the upper stratosphere around 45 km at the other side of the Antarctic continent. This result motivated us to pursue a statistical study on the dominant gravity waves in the stratosphere using the same Fe lidar data in the 30–65-km altitudes (Zhao et al., 2017). An interesting result from the 5-year lidar data is the seasonal variations of vertical wavelength (λ_z), ground-based period (τ), and vertical phase speed (c_z) of the dominant gravity waves in the stratosphere at 30–50 km above McMurdo. Monthly mean λ_z and τ vary from their summer minima (~5.5 km and 4.5 hr) to winter maxima (~8.5 km and 6 hr), while monthly mean c_z remains nearly constant (~0.4 m/s) throughout the year. λ_z and τ exhibit statistically significant linear correlations with the mean background stratospheric winds given by the European Center for Medium-Range Weather Forecasts (ECMWF) model. Based upon the observational result of nearly constant c_z, we assumed in Zhao et al. (2017) that monthly mean horizontal phase speeds were nearly constant over the year and then inferred horizontal wavelengths, intrinsic periods, group velocities, and propagation azimuth and elevation angles. As the inferred horizontal wavelengths of 350–460 km in the stratosphere are much shorter than those of the persistent gravity waves in the MLT (at least 1,000–2,000 km; Chen et al., 2013; Chen & Chu, 2017), we have concluded in Zhao et al. (2017) that the dominant gravity waves in the stratosphere at McMurdo are distinct from the large-scale persistent gravity waves in the MLT. This conclusion is also supported by the fact that the persistent gravity waves in the MLT have much longer vertical wavelengths than the waves in the stratosphere. As noted by Becker and Vadas (2018), wintertime gravity waves in the stratosphere are predominantly orographic or propagating westward. Hence, the vertical wavelengths of these waves decrease with altitude above the polar night jet maximum (in the mesosphere), rather than increase.

A natural conjecture is that the search for persistent wave sources has to continue. Shibuya et al. (2017) have analyzed and simulated the quasi-12 hr IGWs in the lower mesosphere observed by the Program of the Antarctic Syowa MST/IS radar (PANSY radar) at Syowa Station, and they infer that the IGWs are likely generated by spontaneous emission in the regimes of the midlatitude tropospheric jet and the stratospheric polar night jet. This interpretation was suggested by model simulations showing a predominantly vertical flux of westward momentum in the southern winter mesosphere (Shibuya et al., 2017). Very recently, Becker and Vadas (2018) have interpreted the persistent gravity waves during Antarctic winter as secondary gravity waves that are generated in the upper stratosphere and lower mesosphere by wave dissipation-induced horizontal body forces. Here the primary waves originate from the lower atmosphere, likely orographic gravity waves that account for the required intermittency of the body forces that generate the secondary waves. This intriguing picture applies in austral winter at middle and high latitudes. The persistent gravity waves observed in the summer MLT over McMurdo, however, are likely primary nonorographic gravity waves. These waves are probably generated in the troposphere due to the departure from the balanced flow associated with large amplitudes of synoptic-scale Rossby waves. This generation process is commonly called "spontaneous adjustment emission" of gravity wave (e.g., Plougonven & Zhang, 2014; Yasuda et al., 2015). These gravity waves are then filtered by the prevailing wind system in the stratosphere such that only gravity waves with significant eastward phase speeds are relevant in the summer mesosphere (see Becker, 2012; Hoffmann et al., 2010; Lindzen, 1981). It remains to be shown whether the results from general circulation models for summer describe the observed wave properties in the stratosphere and in the MLT. Whatever the gravity wave sources are, the waves emanating from these sources have to satisfy the observed wave properties in both the stratosphere/lower mesosphere and the MLT.

Our current study provides observational characterization of gravity waves in the stratosphere. It is the second part of our statistical study on the stratospheric gravity waves at McMurdo, Antarctica. The first part as mentioned above has been published in Zhao et al. (2017). We now investigate the strength of gravity wave activity in the stratosphere and how it varies through different seasons and over the time span of 5 years from 2011 to 2015.

Gravity waves are known to play essential roles in transporting energy and momentum from the lower to the middle and upper atmosphere and in driving the general circulation of the Earth's atmosphere (e.g., Fritts & Alexander, 2003; Hines, 1960, 1974; Hitchman et al., 1989; Holton, 1982, 1983; Lindzen, 1981). However, the

quantification of gravity wave parameters (such as wavelengths, periods, phase speeds, group velocities, potential and kinetic energy densities, and momentum fluxes) remains a challenge due to the limited number of ground-based observational sites and the limited spatial and temporal resolution of satellite observations (Alexander et al., 2011). Because of the inherent restrictions from different observational instruments, the wide spectra of gravity waves have to be studied with a combination of various observational techniques. Observations will greatly improve the performance of general circulation models through providing the physical basis for more accurate gravity wave parameterization, which is an urgent problem in almost all current general circulation models (e.g., Alexander et al., 2010; Garcia et al., 2014; Geller et al., 2013; Kim et al., 2003; McLandress et al., 2006; Richter et al., 2010). Undoubtedly, satellites can provide global coverage of gravity wave measurements, but it is difficult to infer gravity wave information at very high latitudes near the poles due to the analysis technique and satellite viewing geometry. Ground-based lidar observations with year-round coverage are not bounded by this restriction. Hence, McMurdo lidar observations near 80 °S are irreplaceable in this sense. This lidar has the capability of monitoring gravity waves in the stratosphere, mesosphere, and lower thermosphere (e.g., Chen et al., 2013, 2016; Chu, Huang, et al., 2011; Chu, Yu, et al., 2011; Lu et al., 2015), providing extremely valuable long-term data sets.

Potential energy density is a good indicator of the strength of gravity waves. Here the gravity wave potential energy per unit mass (E_{pm}, i.e., potential energy mass density) is a measure of wave amplitudes, whereas the vertical profile of potential energy per unit volume (E_{pv}, i.e., potential energy volume density) can be used as an indicator of wave dissipation (e.g., Whiteway & Carswell, 1995; Wilson et al., 1991). Yamashita et al. (2009) characterized stratospheric gravity wave activities and compared potential energy densities between Rothera (67.5°S, 68.0°W) and the South Pole (90°S). E_{pm} showed very different seasonal variations at these two sites. At Rothera, E_{pm} variations are characterized by maximum values in winter and minimum values in summer, while E_{pm} remains roughly constant through the year at the South Pole. Following this study, gravity wave activity in the upper stratosphere and lower mesosphere was investigated using temperature data retrieved from Rayleigh lidars at Davis (Alexander et al., 2011; Kaifler et al., 2015). A similar seasonal behavior of E_{pm} as observed at Rothera was reported for Davis. It was unknown how the stratospheric gravity waves behave in the gap region between the South Pole and the Antarctic Circle. Lidar observations at McMurdo fill in this observational gap.

It is worth pointing out that Lu et al. (2015) have done an extensive analysis of McMurdo lidar temperature data for the 2011–2013 winter months (May through August) to study the vertical profiles of potential energy densities and vertical wave number spectra from 35 to 65 km in the Rayleigh region and from 81 to 105 km in the Fe region. They found mean amplitude scale heights of ~10.4 km in the Rayleigh region and ~13.2 km in the Fe region, which are larger than the corresponding atmospheric density scale heights, thus indicative of wave dissipation. The study of Lu et al. (2015) provides a good reference to our current study. We will compute E_{pm} and E_{pv} along with their scale heights in the stratosphere for the complete annual cycle. This will help to assess wave dissipation and its seasonal changes and assist the search for sources of gravity waves in the middle atmosphere.

2. Methodology

2.1. Lidar Observations at Arrival Heights

A lidar observational campaign has been ongoing at Arrival Heights observatory (77.84°S, 166.69°E) near McMurdo, Antarctica, since December 2010 via the collaboration between the United States Antarctic Program and Antarctica New Zealand (Chu, Huang, et al., 2011; Chu, Yu, et al., 2011). An Fe Boltzmann temperature lidar (Chu et al., 2002; Wang et al., 2012) deployed by the University of Colorado Boulder has been recording multiple parameters of the atmosphere from ~15 km to nearly 200 km (e.g., Chen et al., 2013, 2016; Chen & Chu, 2017; Chu et al., 2016, 2011; Chu & Yu, 2017; Chu et al., 2011; Fong et al., 2014, 2015; Lu et al., 2013, 2015, 2017; Yu et al., 2012; Zhao et al., 2017). Analyzed here are the 5 years of lidar temperature data from the pure Rayleigh scattering region (~30–70 km) from 1 January 2011 to 31 December 2015. Over these 5 years, around 5,000 hr of data were collected owing to the dedication of our winter over lidar students (Yu, Roberts, Fong, Chen, and Zhao) and summer-season lidar researchers. The data collection was mainly dictated by weather conditions, and the data distributions in overall 60 months have been tabulated in Zhao et al. (2017). After data screening and division process as described in Zhao et al. (2017), the actual data

Table 1
Statistics on Observational Segments From 2011 to 2015 Employed in the Study

Data duration	Total	12 hr	11 hr	10 hr	9 hr	8 hr	7 hr	6 hr
Number of segments	354	216	32	17	26	22	28	13
Proportion in data points	100%	61.0%	9.0%	4.8%	7.4%	6.2%	7.9%	3.7%
Number of hours (hr)	3798	2592	352	170	234	176	196	78
Proportion in data length	100%	68.2%	9.3%	4.5%	6.2%	4.6%	5.2%	2.0%

used in this study total to 3,798 hr. All the data segments used in this study are between 6 and 12 hr in duration. There are a total of 354 data segments, and the statistics of segment durations are summarized in Table 1. Among them 216 segments have data duration of 12 hr and 32 segments of 11 hr duration, occupying 70% of the data points. Segmenting the data in this way enriches sufficient statistical samples while preserving the persistent gravity waves with periods of 3–10 hr discovered by Chen et al. (2016) in the MLT above McMurdo (see Zhao et al., 2017, for detailed explanations).

The raw photon counts were collected with temporal and altitude resolutions of 1 min and 48 m, respectively. To achieve sufficient signal-to-noise ratios (SNRs) while keeping resolutions as high as possible, the Rayleigh temperature data were retrieved with a temporal integration window of 2 hr and a spatial binning window of 0.96 km. The data retrieval was done with the oversampling method to have display resolutions of 1 hr and 0.96 km. We chose the altitude range of 30–50 km in order to achieve sufficiently high SNRs in summer (when solar background noise is largest) for the studies covering the entire year.

2.2. Derivation of Potential Energy Densities

The derivation of E_{pm} and E_{pv} consists of two major courses. The first course is to derive gravity wave perturbations from the raw temperature data that are affected by a variety of atmospheric waves (e.g., planetary, tidal, and gravity waves), and the second course is to accurately estimate the energy of gravity waves from the derived gravity wave perturbations that also include noise contributions. Here we use summer lidar observations on 31 December 2014 as an example to illustrate the data processing procedures employed. The 12 temperature profiles from 30 to 50 km measured on that day are plotted in Figure 1A$_1$, while the corresponding temperature contour is plotted in Figure 1A$_2$. Temperatures generally increase from ~240 K at 30 km to ~280–290 K at 50 km. Typical measurement errors increase from ~0.2 to 6 K from 30 to 50 km in summer but are much smaller (~0.1 to 1 K) in winter. Two-dimensional fast Fourier transform (2DFFT) applied to the raw temperature data reveals dominant DC components (corresponding to mean temperature background fields with zero frequency and zero vertical wave number) in the power spectral density (see Figure 1A$_3$).

2.2.1. Deriving Overall Gravity Wave Perturbations From Raw Temperatures

The first course in the derivation aims to remove the DC background to reveal wave perturbations and remove waves outside the gravity wave spectra of interest. This is accomplished via a combination of background subtractions and applications of filters. Briefly, temperature perturbations $\Delta T(z, t)$ are calculated by first subtracting the temporal background $T_0(z)$ of the observational segment at each altitude and then subtracting the spatial background over the altitudes of 30–50 km at each time grid for every observational segment. Following the background subtractions, at each individual altitude, a sixth-order Butterworth high-pass filter is applied to the temperature perturbations obtained above to remove waves with periods longer than 11 hr. At each individual time grid, such temporally filtered temperature perturbations are run through a sixth-order Butterworth high-pass filter to remove waves with vertical wavelengths longer than 30 km. The obtained final temperature perturbations $T'(z, t)$ are then converted to the filtered relative temperature perturbations of every observational segment as

$$T'_{Rel}(z, t) = T'(z, t)/T_0(z) \tag{1}$$

Note that our goal here is not to extract individual gravity waves but to derive the overall perturbations caused by gravity waves whose spectra fall within the spectral range of interest.

Let us illustrate how each step is done in the data analysis procedure described above and how the procedure affects the wave spectra.
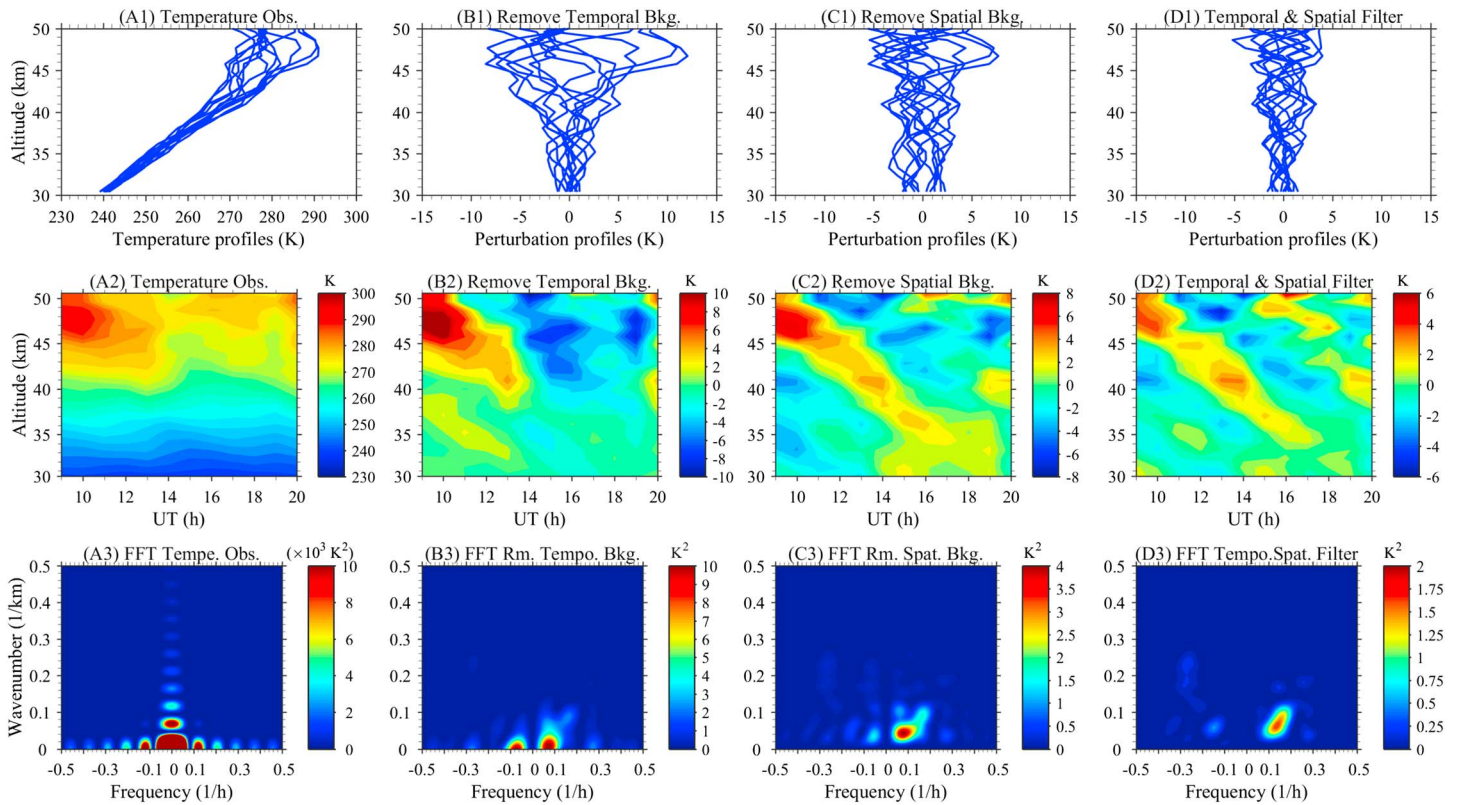
Figure 1. Lidar observations on 31 December 2014 at McMurdo are used as an example to illustrate the procedures of extracting gravity wave perturbations from the raw temperature data. (first row) temperature profiles, (second row) temperature contours, and (third row) power spectral density (PSD) of 2-D FFT. (A column) Raw temperature profiles along with their corresponding temperature contour and 2-D FFT PSD. (B column) Temperature perturbation profiles, contour, and 2-D FFT PSD after temporal background subtraction. (C column) Same as B column except after temporal and spatial background subtractions. (D column) Same as B column except after temporal and spatial filtering following the temporal and spatial background subtractions. Note that the color scales for (A3) are 3–4 orders of magnitude larger than those in (B3)–(D3).

1. The temporal background $T_0(z)$ is estimated as the temporal mean over the time span of the observation segment. Subtraction of $T_0(z)$ leads to the removal of the DC term and long-period (low-frequency) waves in the frequency spectra. Note that the revealed wave spectra in Figure 1B$_3$ have much smaller power densities than those of the DC and long-period spectra in Figure 1A$_3$. The corresponding temperature perturbations and contour are plotted in Figures 1B$_1$ and 1B$_2$. Comparing two contour plots in Figures 1A$_2$ and 1B$_2$, we can see that the raw temperatures are dominated by long-period waves (most likely planetary waves; Lu et al., 2013, 2017), while shorter-period waves begin to show up in Figure 1B$_2$.

2. The spatial background is estimated as the running mean over the altitude range of 30–50 km obtained with a 30-km sliding window. For any altitude within the 30–50 km range, the arithmetic mean over its vicinity of ±15 km (i.e., 30-km window width) is taken as the spatial background at this altitude. (When taking the average within the 30-km window, altitude bins outside the observational range are ignored.) As the window slides along the altitude, different altitudes may have different spatial backgrounds, which are different from the traditional practice where a vertical mean over the observational range is used as the spatial background for all altitudes within the 30–50 km range (e.g., Zhao et al., 2017). Subtraction of the spatial background removes the DC term and waves with long vertical wavelengths (small vertical wave numbers) in the vertical wave number spectra (Figure 1C$_3$). Figure 1C$_1$ shows more confined gravity wave perturbation profiles than Figure 1B$_1$, while gravity wave signatures become clear in Figure 1C$_2$.

3. After the background subtractions there is still considerable energy in the spectral range with periods longer than 11 hr and vertical wavelengths longer than 30 km (Figure 1C$_3$), possibly leakage from the DC term and waves with long periods and long vertical wavelengths. Therefore, two sixth-order Butterworth high-pass filters are then applied in the temporal and spatial domains, respectively, to reduce the spectral energy of these waves. To apply these two filters, the original data segments are zero-padded

to 128 hr and 128 km, respectively, before the time series or spatial series are run through the 1-D FFT. Zero-padded data spectra are multiplied by the sixth-order Butterworth high-pass filter functions point by point, and then the filtered spectra are run through 1-D inverse FFT to convert back to the time or spatial domain. The filtered perturbations are illustrated in Figure 1D$_2$, and their spectra are shown in Figure 1 D$_3$. The temporal filter retains 50%, 78.4%, 93.1%, and 98.4% of the energy of waves with periods of 11, 10, 9, and 8 hr, respectively. The spatial filter retains 50%, 90%, and 99.4% of the energy of waves with vertical wavelengths of 30, 25, and 20 km, respectively. The 3-dB cutoff period and vertical wavelength are 11 hr and 30 km for these temporal and spatial filters, respectively. They are set to preserve the IGW spectra (Chen et al., 2013, 2016; Chen & Chu, 2017) as fully as possible while significantly removing semidiurnal tides, diurnal tides, and planetary wave components with periods over 1 day and vertical wavelengths over 40 km that are dominant in the stratosphere (Lu et al., 2013, 2017).

4. We do not extract individual gravity waves using the above procedure. Instead, the filtered relative temperature perturbations (Figures 1D$_1$ and 1D$_2$) represent the perturbations induced by gravity waves with periods of 3–11 hr and vertical wavelengths of 2–30 km (see Figure 1D$_3$). Here the major contributions of energy come from gravity waves with periods of 3–9 hr and vertical wavelengths of 2–20 km. As shown in Table 1, ~70% data segments have durations of 11–12 hr, which, before the application of the temporal high-pass filter, allow the inclusion of nearly full energy of gravity waves with periods of 4–11 hr and partial energy of gravity waves with periods of 2–4 hr (because the temporal integration is 2 hr for raw temperatures) and from the segment lengths up to twice the segment lengths. The temporal high-pass filter attenuates partial energy of waves with periods of 11 and 10 hr but keeps the majority of energy of waves with periods shorter than 9 hr. The short duration (6–7 hr) segments occupy only ~7% of the total data length (see Table 1), but they still include partial energy of gravity waves with periods from 6–7 hr up to twice the segment lengths (12–14 hr). The temporal high-pass filter further attenuates waves with periods longer than 9 hr. Similarly, before the application of the spatial high-pass filter, the 20-km data window from 30 to 50 km contains the nearly full energy of gravity waves with vertical wavelengths of 2–20 km (the spatial integration is 0.96 km for raw temperatures) and partial energy of gravity waves with vertical wavelengths from 20 km up to twice the window length (40 km). The spatial high-pass filter attenuates partial energy of waves with vertical wavelengths longer than 25 km but has almost no effects on the 2–20-km waves. Therefore, gravity waves with periods of 3–9 hr and vertical wavelengths of 2–20 km are the major energy contributors to the wave perturbations derived above, while gravity waves with periods of 9–11 hr and vertical wavelengths of 20–30 km also contribute partial energy to the perturbations.

There are some limitations to our procedure described above, mainly due to the limited duration of some data segments. We have used zero padding on data segments to allow the estimation of gravity waves with periods longer than the original data lengths, for example, extracting 11-hr period waves from 6-hr data duration. However, the period determination in such cases may be sometimes biased toward shorter periods and sometimes biased toward longer periods, depending on the phase of the superimposed longer-period planetary waves. As the gravity wave potential energy densities derived in the following sections are not divided into individual wave periods but integrated over the allowable spectra, the uncertainties in wave period determination are unlikely to bias the total potential energy densities. In fact, we have tested to remove these short-duration data segments (41 out of 354) that are only a small fraction of the entire data set and computed the potential energy density profiles, histograms, and seasonal variations again (not shown). The results are nearly identical to the original results using the full 354 data segments, demonstrating the robustness of our data analysis results. The majority of our data segments is longer than 11 hr. Our methods derive accurate periods of 3–9-hr waves for data segments of 12 and 11-hr duration, although the 10–11-hr gravity waves could appear with slightly shorter periods than expected, according to our forward modeling. We choose to include the 41 data segments with duration of 6 and 7 hr because these data segments increase the data statistics, making the potential energy density profiles smoother than without them.

2.2.2. Accurately Estimating Gravity Wave Potential Energy Densities

The second course is to further analyze these gravity wave perturbations to derive E_{pm} and E_{pv}, removing the contamination from noise contributions. For each observational segment, the altitude profile of gravity wave potential energy mass density $E_{pm}(z)$ is calculated from the filtered temperature perturbations $T'(z, t)$ using equation (2) (e.g., Duck et al., 2001; Yamashita et al., 2009).

$$E_{pm}(z) = \frac{1}{2}\frac{g^2}{N^2(z)}\overline{\left(\frac{T'_{GW}(z,t)}{T_{Bkg}(z)}\right)^2} = \frac{1}{2}\frac{g^2}{N^2(z)}\frac{1}{N_p}\sum_{i=1}^{N_p}\left(\frac{T'_{GW}(z,t_i)}{T_{Bkg}(z)}\right)^2 \tag{2}$$

where the overbar denotes taking the mean over the time span of the observational segment, $g = 9.7$ m/s^2 is the gravitational acceleration corresponding to the stratosphere, z and t respectively represent altitude and time, T_{Bkg} is the monthly mean background temperature, and N_p is the number of temperature perturbation profiles within the segment time span. Here $N(z)$ is the buoyancy frequency calculated from the segment temporal mean temperatures $T_0(z)$ through

$$N^2(z) = \frac{g}{T_0(z)}\left(\frac{dT_0(z)}{dz} + \frac{g}{C_p}\right) \tag{3}$$

where $C_p = 1{,}004$ J/K/kg is the specific heat of dry air at constant pressure. In equation (2) T'_{GW} represents the pure temperature perturbations induced by gravity waves, and its mean square should be calculated, in principle, from $T'(z,t)$ by removing the noise variance.

$$\overline{\left[T'_{GW}(z,t)\right]^2} = \overline{\left[T'(z,t)\right]^2} - \overline{\left[\sigma_T(z,t)\right]^2} \tag{4}$$

where the overbars represent taking the mean over the time span of the observational segment, $T'(z,t)$ is the filtered temperature perturbation as derived in section 2.2.1, and $\overline{\left[\sigma_T(z,t)\right]^2}$ is the noise variance due to the temperature uncertainty caused by photon noise.

How to accurately estimate noise variance deserves careful considerations. Duck et al. (2001) calculated the noise variance as

$$\overline{\left[\sigma_T(z,t)\right]^2} = \sigma_T^2(z) = \frac{1}{N_p}\sum_{i=1}^{N_p}\left[\delta T(z,t_i)\right]^2 \tag{5}$$

where $\delta T(z,t_i)$ is the filtered uncertainty of the measured temperature profile. Such subtraction method is best suited for nighttime lidar measurements when the temperature measurement uncertainty is small compared to the gravity wave-induced temperature perturbation. In this case, the error in measurement uncertainty estimation is negligible and will not substantially alter the derived $E_{pm}(z)$. However, under full sunlight in Antarctic summer, the magnitude of temperature uncertainty can become so large that it is close to or even exceeds that of the gravity wave-induced temperature perturbation at high altitudes. Due to the error in the uncertainty estimation, the noise variance as calculated by equation (5) can become unreliable and even lead to negative values for $E_{pm}(z)$ when using equations (4) and (2). To overcome this issue, we develop a spectral proportion method that combines Fourier spectral analysis at each altitude with Monte Carlo simulations to estimate the proportion of gravity wave energy occupying the total spectral energy and then scale the $T'(z,t)$ square with this proportion. Let $p(z)$ represent this gravity wave proportion at altitude z, the mean square of pure temperature perturbations induced by gravity waves and the noise variance are then computed as

$$\overline{\left[T'_{GW}(z,t)\right]^2} = \overline{\left[T'(z,t)\right]^2}\cdot p(z)$$
$$\overline{\left[\sigma_T(z,t)\right]^2} = \overline{\left[T'(z,t)\right]^2}\cdot[1-p(z)] \tag{6}$$

The uncertainty associated with $E_{pm}(z)$ is calculated following the same procedure as in Whiteway and Carswell (1995), but the estimate of noise variance is updated with equation (6) to

$$\delta E_{pm}(z) = \frac{1}{2}\frac{g^2}{N^2(z)}\overline{\left[\frac{\sigma_T(z,t)}{T_{Bkg}(z)}\right]^2}\frac{1}{\sqrt{N_p}} = \frac{1}{2}\frac{g^2}{N^2(z)}\overline{\left[\frac{T'(z,t)}{T_{Bkg}(z)}\right]^2}\cdot[1-p(z)]\frac{1}{\sqrt{N_p}}. \tag{7}$$

Here the gravity wave proportion $p(z)$ is estimated with the following Monte Carlo procedure. We first construct 1,000 sets of 2-D temperature map (temperature versus time and altitude) with Gaussian white
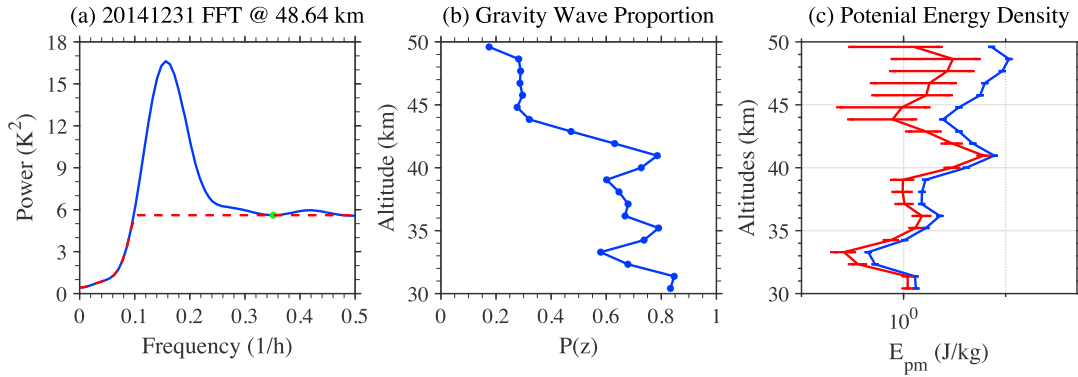
Figure 2. Illustration of the spectral proportion method using lidar observations on 31 December 2014 at McMurdo as an example. (a) The mean power spectral density over 1,000 Monte Carlo simulated time series at an altitude of 48.64 km. The red dashed line marks the noise floor over the frequency spectra. (b) The gravity wave proportion $p(z)$ profile determined with equation (8) for this day of lidar observations. (c) Blue curve represents the total potential energy mass density including noise contributions, and the red curve represents the pure gravity wave $E_{pm}(z)$ profile obtained with the spectral proportion method. The horizontal lines denote the error bars associated with the derived $E_{pm}(z)$.

noise added to the lidar-measured raw temperatures; that is, the standard deviation of the added noise is equal to the raw measurement error at each grid point. Second, we run each of the so-constructed 2-D temperature maps through the same processing procedure as described in section 2.2.1 (background subtraction and filtering processes) to obtain filtered temperature perturbation fields. Then at each altitude we calculate the 1-D FFT power spectra for each time series of the 1,000 filtered temperature perturbations and take the mean of these 1,000 spectra of 1-D FFT to estimate the spectral noise floor. An example is shown in Figure 2a for lidar observations on 31 December 2014 at an altitude of 48.64 km. The dashed red line indicates the noise floor at various frequencies. Finally, we integrate the power spectral density (PSD) above and below the spectral noise floor to obtain the wave and noise areas, respectively, and then derive the gravity wave proportion as

$$p(z) = \frac{\text{wave area in PSD}}{\text{wave area} + \text{noise area}}. \tag{8}$$

As $p(z)$ varies only between 0 and 1 (see Figure 2b), the derived $E_{pm}(z)$ using equations (2) and (6) will never be negative (see Figure 2c), thus overcoming the issues associated with the noise variance subtraction method. Tests with forward modeled data and then with real lidar data have shown that for Antarctic winter cases with small error bars, the spectral proportion method and the noise variance subtraction method give nearly identical profiles of $E_{pm}(z)$, demonstrating the effectiveness of this new method in handling both small and large error cases.

We also compute the altitude profile of gravity wave potential energy volume density $E_{pv}(z)$, for each observational segment, by multiplying $E_{pm}(z)$ with the background atmospheric density $\rho_0(z)$:

$$E_{pv}(z) = \rho_0(z)E_{pm}(z). \tag{9}$$

Here the background atmospheric density can be taken from an empirical model such as NRLMSISE-00 (Picone et al., 2002) or determined from the lidar measurements of Rayleigh scattering signals. The latter choice involves first deriving the relative atmospheric density via taking Rayleigh normalization (Chu & Papen, 2005) at a prechosen altitude z_N, say 45 km, and then converting to the absolute atmospheric density via scaling the relative density profile with atmospheric density at z_N taken from the empirical model NRLMSISE-00 (e.g., Chu & Papen, 2005; Gardner et al., 1989; Hauchecorne et al., 1992). Although the absolute density values still depend on an empirical model, the relative density profiles, which determine the shape of E_{pv} profiles, are given by the real lidar measurements. The corresponding error bars are estimated as

$$\delta E_{pv}(z) \approx \sqrt{\rho_0^2(z)\delta E_{pm}^2(z) + E_{pv}^2(z)\frac{N_{\text{Total}}(z)}{[N_{\text{Total}}(z) - B]^2}}, \tag{10}$$
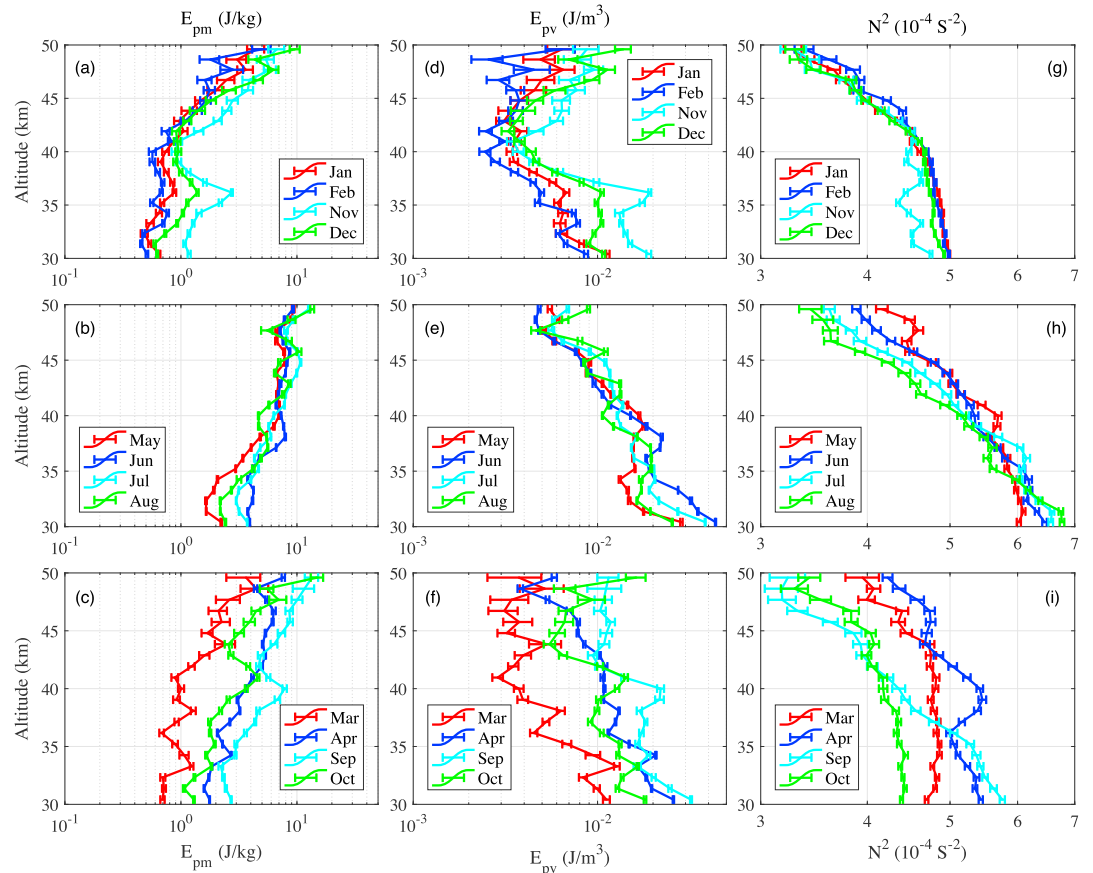
Figure 3. Five-year (2011–2015) monthly mean vertical profiles of (left column) E_{pm}, (middle column) E_{pv}, and (right column) N^2 with error bars for (top) summer months (November through February), (middle) winter months (May through August), and (bottom) fall/spring months (March, April, September, and October) at McMurdo, Antarctica. Error bars represent the errors of monthly mean profiles, which are computed from the errors of individual segment profiles via error propagation.

where N_{Total} is the total photon count at altitude z and B is the estimated background count. Our tests show that the empirical model density and the lidar-measured density give similar results of E_{pv} profiles, so we choose to use the empirical model density and simplify the error estimation to

$$\delta E_{pv}(z) \approx \rho_0(z) \delta E_{pm}(z). \tag{11}$$

3. Vertical Profiles of E_{pm} and E_{pv} Along With Their Scale Heights

$E_{pm}(z)$ vertical profiles are derived for all the qualified segments following the procedures described above, and then $E_{pm}(z)$ in the same months are averaged over the 5 year span to obtain the monthly mean $E_{pm}(z)$ profiles for each of the 12 months through a year. The errors of monthly mean $E_{pm}(z)$ profiles are computed from the errors of individual $E_{pm}(z)$ profiles via error propagation. The results are shown as three separated groups in the left column of Figure 3: summer (November through February), winter (May through August), and spring/fall (September-October/March-April). Similar analyses are done for $E_{pv}(z)$ and $N^2(z)$, and the results are shown in the middle and right columns of Figure 3. Using logarithmic scales, $E_{pm}(z)$ profiles increase with altitude, while $E_{pv}(z)$ profiles decrease with altitude, in general. The increasing and decreasing rates vary from month to month. We quantify such variations via the scale heights H_{pm} and H_{pv} of $E_{pm}(z)$ and $E_{pv}(z)$ as defined below (e.g., Lu et al., 2015):
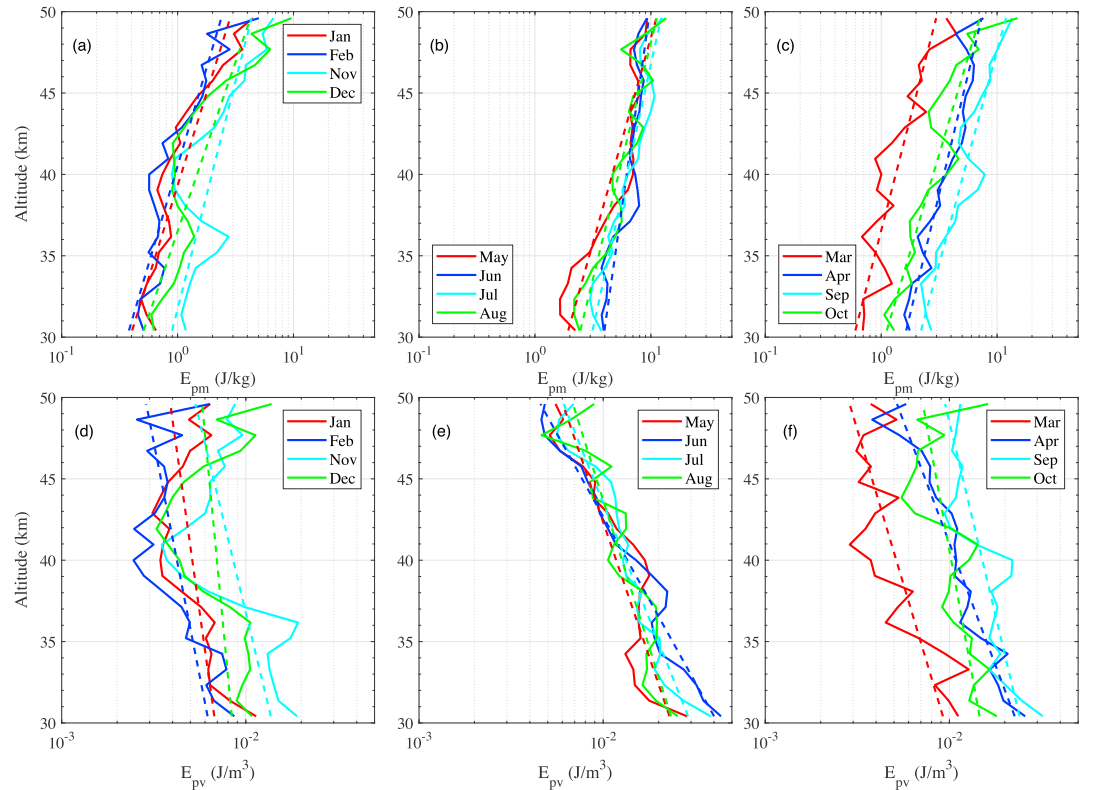
Figure 4. Linear fits (dashed lines) to the vertical profiles (solid lines) of (top panel) E_{pm} and (bottom panel) E_{pv} for summer months (November through February) on the left, winter months (May through August) in the middle, and fall/spring months (March, April, September, and October) on the right at McMurdo, Antarctica.

$$E_{pm}(z) = E_{pm}(z_0) \exp\left(\frac{z - z_0}{H_{pm}}\right) \Rightarrow \ln\left[E_{pm}(z)\right] - \ln\left[E_{pm}(z_0)\right] = (z - z_0)/H_{pm}, \tag{12}$$

$$E_{pv}(z) = E_{pv}(z_0) \exp\left(\frac{z - z_0}{H_{pv}}\right) \Rightarrow \ln\left[E_{pv}(z)\right] - \ln\left[E_{pv}(z_0)\right] = (z - z_0)/H_{pv}. \tag{13}$$

Figure 4 illustrates the linear fits to the logarithmic $E_{pm}(z)$ and $E_{pv}(z)$ profiles using equations (12) and (13). The scale heights determined from the linear fits are summarized in Table 2 along with the atmospheric density scale height H. Under the definitions of equations (13), negative H_{pv} indicates the decrease of $E_{pv}(z)$ with increasing altitude. These scale heights are indicators for the dissipation of gravity wave energy: Assuming that the background wind and the static stability do not change with altitude (constant vertical wavelength), E_{pv} remains constant with altitude for a conservative gravity wave and decreases with altitude when wave dissipation occurs (Whiteway & Carswell, 1995; Wilson et al., 1991). Thus, for a monochromatic upward propagating gravity wave, the absolute magnitude of H_{pv} is infinity if the wave is nondissipative and its vertical wavelength is constant with height, but H_{pv} is negative and finite if the wave dissipates. The smaller the absolute magnitude of H_{pv}, the faster the wave dissipates with altitude. Likewise, a positive H_{pm} larger than the atmospheric density scale height H means that E_{pm} grows with altitude more slowly than a monochromatic conservative wave, with larger positive values of H_{pm} indicating stronger dissipation (Lu et al., 2015; Mzé et al., 2014). However, the actual situations are much more complicated than this simple picture because the observed potential energy densities are the sum of contributions from multiple gravity waves generated by various sources at multiple heights and locations. Furthermore, when the mean wind varies slowly with height (which is usually the case), only are the energy flux density and momentum flux density constant with altitude for a monochromatic and conservative gravity wave, but the potential and kinetic energy densities are not necessarily constant (Becker & Vadas, 2018). The obtained $E_{pm}(z)$ and $E_{pv}(z)$ in Figure 3 show

Table 2
Scale Heights (H_{pm} and H_{pv}) of E_{pm} and E_{pv} Profiles

	Jan	Feb	Mar	Apr	May	Jun	Jul	Aug	Sep	Oct	Nov	Dec
H_{pm} (km)	9.9 ± 0.9	10.5 ± 1.0	12.0 ± 1.2	12.8 ± 0.9	11.0 ± 1.0	21.7 ± 2.2	14.1 ± 1.1	12.6 ± 1.1	11.4 ± 0.9	10.4 ± 1.0	12.2 ± 1.4	9.0 ± 1.0
H_{pv} (km)	−34.8 ± 7.3	−25.0 ± 5.8	−16.4 ± 3.8	−13.0 ± 1.8	−14.4 ± 2.8	−8.8 ± 0.8	−12.3 ± 1.6	−15.7 ± 3.1	−20.6 ± 4.5	−27.0 ± 6.3	−20.3 ± 4.5	−51.8 ± 6.1
H (km)	−7.73 ± 0.12	−7.44 ± 0.11	−6.99 ± 0.12	−6.52 ± 0.13	−6.28 ± 0.15	−6.33 ± 0.17	−6.61 ± 0.18	−7.02 ± 0.19	−7.36 ± 0.18	−7.56 ± 0.16	−7.69 ± 0.15	−7.77 ± 0.13

Note. Positive (negative) scale heights denote the cases of corresponding parameters increasing (decreasing) with increasing altitude. The signs of ± denote the standard errors.

complicated profiles; for example, $E_{pv}(z)$ profiles in summer months decrease with altitude first and then increase or become nearly vertical, reflecting the interplay of multiple factors. Because of this complication, we choose not to further study the turning features in the summer $E_{pv}(z)$ profiles but rather apply simple linear fits to quantify the slopes. The H_{pv} values in Table 2 indicate that the wave dissipation in winter is much more severe than that in summer in the altitude range of 30–50 km.

4. Statistics and Lognormal Distributions of E_{pm} and E_{pv}

The altitude mean $\overline{E}_{pm}$ of gravity wave potential energy mass density from 30 to 50 km is derived for each observational segment as

$$\overline{E}_{pm} = \frac{1}{N_z} \sum_{k=1}^{N_z} E_{pm}(z_k), \tag{14}$$

and the associated error bar is reduced to

$$\delta\overline{E}_{pm} = \frac{1}{N_z} \sqrt{\sum_{k=1}^{N_z} \left[\delta E_{pm}(z_k) \right]^2}. \tag{15}$$

where N_z is the number of data points within an altitude profile. The altitude mean $\overline{E}_{pv}$ of gravity wave potential energy volume density from 30 to 50 km and associated error are derived for each observational segment as

$$\overline{E}_{pv} = \frac{1}{N_z} \sum_{k=1}^{N_z} E_{pv}(z_k). \tag{16}$$

$$\delta\overline{E}_{pv} = \frac{1}{N_z} \sqrt{\sum_{k=1}^{N_z} \left[\delta E_{pv}(z_k) \right]^2}. \tag{17}$$

We obtain 354 data points of $\overline{E}_{pm}$ for all the qualified data through 5 years and the same number of data points for $\overline{E}_{pv}$. Here each data point represents one observational segment. The mean $\overline{E}_{pm}$ and $\overline{E}_{pv}$ along with their standard deviations are summarized in Table 3 for the entire data set and for summer, winter, and spring/fall. $\overline{E}_{pm}$ and $\overline{E}_{pv}$ histograms for all 354 data points are plotted in Figures 5a and 5f, respectively. These distributions are skewed and deviate significantly from normal distributions. $\overline{E}_{pm}$ and $\overline{E}_{pv}$ histograms are fitted with the lognormal distribution.

$$h(x) = \frac{A}{\sqrt{2\pi}\sigma} \exp\left[-\frac{(\ln x - \mu)^2}{2\sigma^2} \right]. \tag{18}$$

The fitting parameters μ, σ, and A are listed in Table 3. The correlation coefficients for the lognormal fittings are very high, 0.97 and 0.99 for $\overline{E}_{pm}$ and $\overline{E}_{pv}$, respectively, at 95% confidence levels. Therefore, the mean $\overline{E}_{pm}$ and $\overline{E}_{pv}$ between 30 and 50 km are lognormally distributed at McMurdo. The most probable value (MPV) is given by $x_{MPV} = e^{\mu}$, which is 1.29 J/kg and 5.2×10^{-3} J/m^3 for $\overline{E}_{pm}$ and $\overline{E}_{pv}$, respectively, as summarized in Table 3. $\overline{E}_{pm}$ ranges from less than 1 to nearly 20 J/kg, and $\overline{E}_{pv}$ ranges from 1.4×10^{-3} to 4.5×10^{-2} J/m^3; however, the lognormal distribution indicates that most $\overline{E}_{pm}$ and $\overline{E}_{pv}$ values are small.

Dividing the $\overline{E}_{pm}$ data into seasons, we plot the histograms for summer, spring/fall, and winter distributions in Figures 5b–5d. The differences among seasons are striking—the summer $\overline{E}_{pm}$ are clustered in a narrow band of low values (with a MPV of 1.06 J/kg and ranging mainly from 0.2 to 4 J/kg) with a nearly perfect lognormal distribution at 0.99 correlation, while the winter $\overline{E}_{pm}$ shifts the MPV to ~3.2 J/kg and exhibits a very wide distribution range. The spring/fall distribution lies in between the summer and winter cases with intermediate MPV and distribution width. It is worth pointing out from Figure 5 that most of the large $\overline{E}_{pm}$ values

Table 3
Data Statistics and Lognormal Fitting Parameters to $\overline{E}_{pm}$ and $\overline{E}_{pv}$ Histograms

$\overline{E}_{pm}$(J/kg)	Total data points	Mean ± Std. deviation	μ	σ	A	Correlation	MPV
Total	354	3.82 ± 3.42	0.253	0.81	93.98	97%	1.29
Summer	142	1.84 ± 1.35	0.055	0.60	55.56	99%	1.06
Winter	122	6.16 ± 3.82	1.158	0.63	15.28	82%	3.18
Spring + fall	90	3.76 ± 3.16	0.406	0.75	21.97	92%	1.50

$\overline{E}_{pv}(10^{-2}$ J/m^3)	Total Data Points	Mean ± Std. Deviation	μ	σ	A	Correlation	MPV
Total	354	1.08 ± 0.85	−5.25	0.65	104.71	99%	0.52
Summer	142	0.71 ± 0.46	−5.48	0.60	56.57	99%	0.42
Winter	122	1.48 ± 0.99	−4.86	0.49	24.01	91%	0.77
Spring + fall	90	1.13 ± 0.87	−5.25	0.72	26.48	95%	0.52

(>9 J/kg) in the overall lognormal distribution (Figure 5a) occur in the winter season. In contrast, the small $\overline{E}_{pm}$ values (<1 J/kg) in Figure 5a receive very minor contributions from the winter season but occur mainly during summer. Lognormal distributions given by equation (18) are also fit to the seasonal histograms, and the fitting parameters are summarized in Table 3. Again, the correlation coefficients are high, ranging from
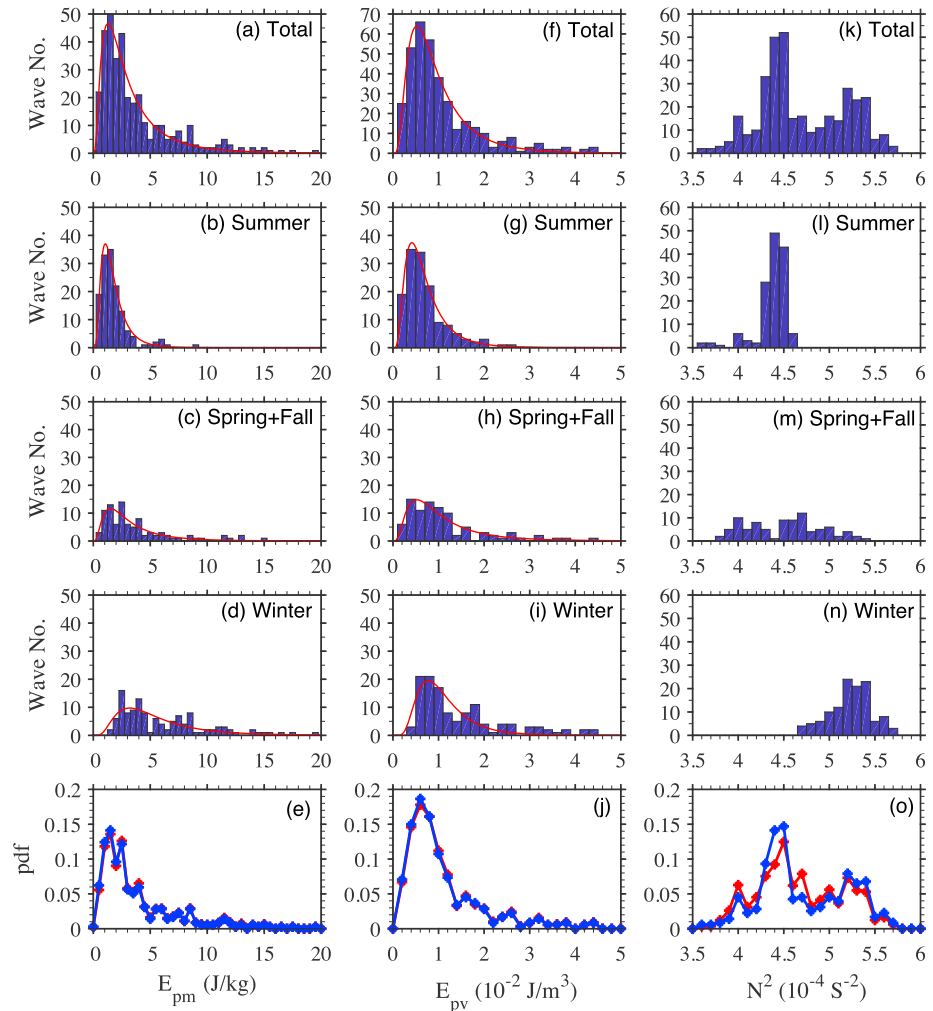

Figure 5. Lognormal distribution of (left column) altitude mean $\overline{E}_{pm}$, (middle column) lognormal distribution of altitude mean $\overline{E}_{pv}$, and (right column) distribution of altitude mean $\overline{N^2}$ in the whole year, summer, spring/fall, and winter seasons from the first to the fourth rows. The bottom row shows the comparison of the original (blue) and normalized (red) distributions of $\overline{E}_{pm}$, $\overline{E}_{pv}$, and $\overline{N^2}$.
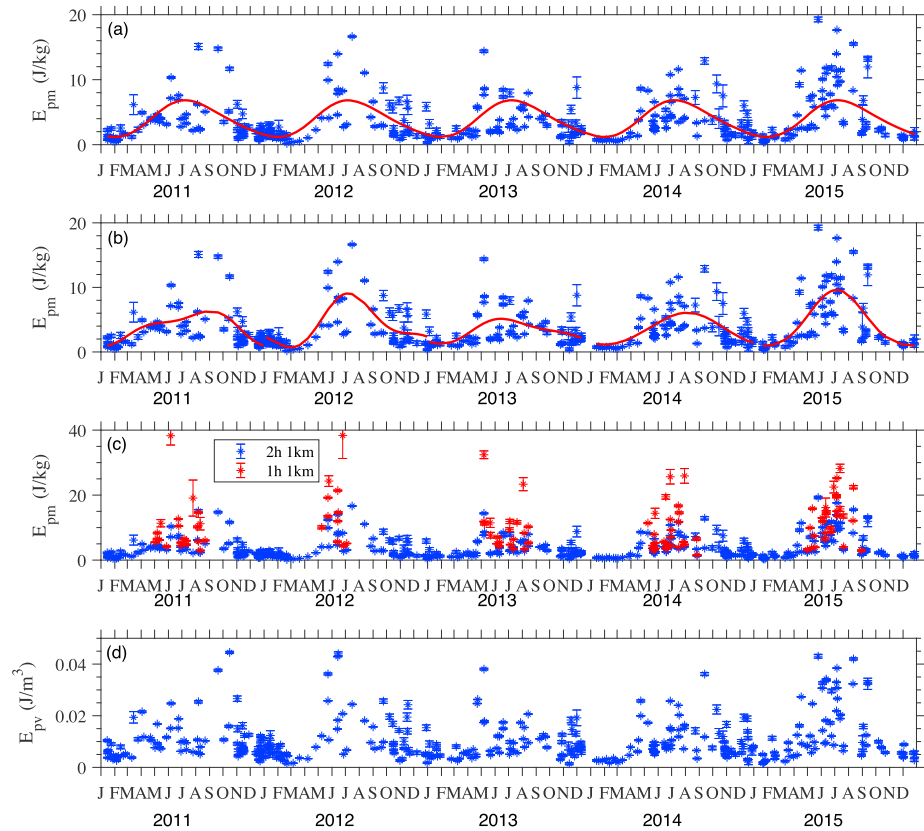
Figure 6. (a–c) Altitude mean $\overline{E}_{pm}$ (J/kg) and (d) altitude mean $\overline{E}_{pv}$ (J/m^3) averaged over the 30–50-km altitude range for all the observations over 5 years from 2011 to 2015. The blue asterisks in all panels denote the actual $\overline{E}_{pm}$ or $\overline{E}_{pv}$ observation at temporal and spatial resolutions of 2 hr and 1 km during single observational segments with their errors calculated using equations (15) and (17). The red lines are (a) overall annual + semianuual fits for 5 years and (b) single year annual + semianuual fits for five individual years, respectively. The red dots in (c) are the $\overline{E}_{pm}$ derived under a higher temporal resolution of 1 hr (only for winter months).

0.82 in winter to 0.99 in summer. The annual cycle of $\overline{E}_{pm}$ (with summer minima and winter maxima) clearly shows up in the most probable values. Because of the large width of the distributions for $\overline{E}_{pm}$ during winter, the 122 data points in this case are less ideal for our statistics, and more data points would increase the correlation. The spring/fall seasons have only 90 data points, which is also less ideal than the summer case with 142 points distributed in a narrow range. The distributions of $\overline{E}_{pv}$ seasonal histograms (Figures 5g–5i) are similar to those of $\overline{E}_{pm}$ as demonstrated in the middle column of Figure 5.

Histograms of altitude mean $\overline{N^2}$ of total 354 data points and of summer, winter, and spring/fall seasons are plotted in the right column of Figure 5. Apparently, $\overline{N^2}$ does not obey a lognormal distribution. A striking feature in the year-round distribution is the two independent peaks corresponding to summer and winter, respectively. Summer $\overline{N^2}$ clusters narrowly around 4.4×10^{-4} s^{-2}, whereas winter $\overline{N^2}$ distributes in a much wider range from 4.7×10^{-4} to 5.7×10^{-4} s^{-2}, centering around 5.25×10^{-4} s^{-2}. The two peaks in Figure 5m correspond to spring and fall. Spring has lower $\overline{N^2}$ values than the summer peak, while fall $\overline{N^2}$ values are between summer and winter. The fall peak of $\overline{N^2}$ is higher than that during spring by $\sim 0.6 \times 10^{-4}$ s^{-2}. Considering that different seasons have different numbers of data, which may affect the overall distribution of $\overline{N^2}$, we normalize each season with its number of data points and then combine all seasons together. Such normalized results are compared with the original probability density function (PDF) in Figure 5o. The $\overline{N^2}$ distribution does change somewhat from the original PDF, but it is still not a lognormal distribution. The similar normalization procedure is applied to $\overline{E}_{pm}$ and $\overline{E}_{pv}$, and the results are compared with the
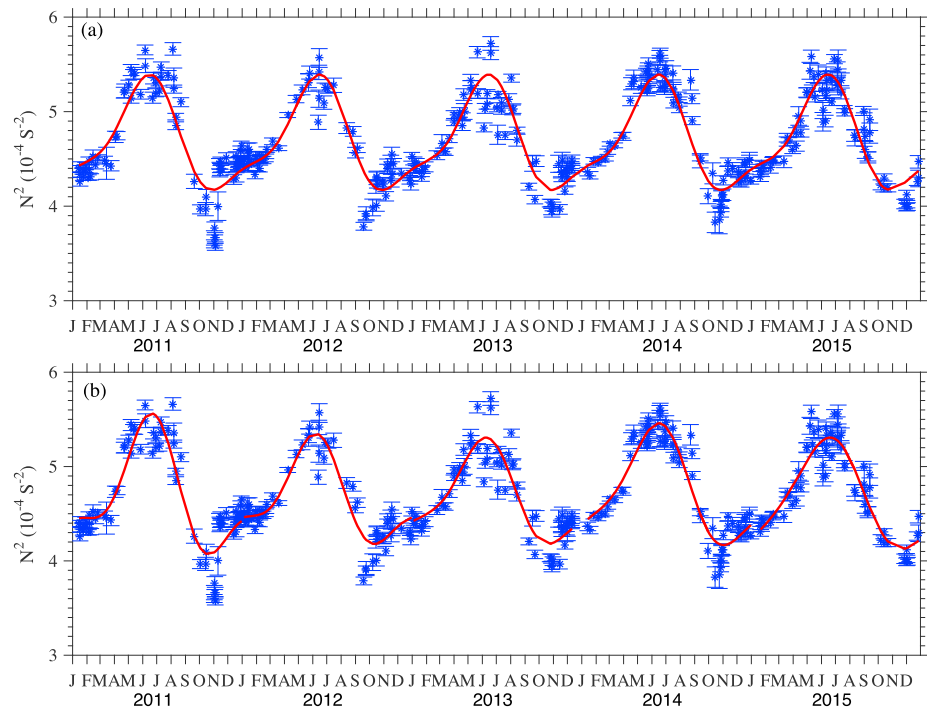
Figure 7. Altitude mean $\overline{N^2}$ from 30 to 50 km through five years of 2011–2015. Each blue asterisk denotes a single observational segment with error bar. The red lines are (a) overall annual + semianuual fits for 5 years and (b) single year annual + semianuual fits for five individual years, respectively.

original $\overline{E}_{pm}$ and $\overline{E}_{pv}$ in Figures 5e and 5j. Obviously, the normalized $\overline{E}_{pm}$ and $\overline{E}_{pv}$ distributions are nearly identical to the original PDFs and closely resemble the lognormal distributions. Lognormal distributions of $\overline{E}_{pm}$ and $\overline{E}_{pv}$ observed by the lidar are in good agreement with radiosonde and satellite observations that reveal lognormal distributions of gravity wave potential energy density and momentum flux (Alexander et al., 2008; Baumgaertner & McDonald, 2007; Hertzog et al., 2012; Murphy et al., 2014); however, we are not aware of previous observations of $\overline{N^2}$ distributions.

5. Seasonal and Interannual Variations of E_{pm} and E_{pv}

We now investigate how $\overline{E}_{pm}$, $\overline{E}_{pv}$, and $\overline{N^2}$ vary with time. All the 354 data points of $\overline{E}_{pm}$ and $\overline{E}_{pv}$ are plotted as a function of day of year (DOY) in Figures 6a and 6d, ranging from 1 January 2011 to 31 December 2015. Each data point represents the measurements of one 12-hr segment, and the error bars are the associated $\delta\overline{E}_{pm}$ and $\delta\overline{E}_{pv}$ computed with equations (15) and (17). An obvious and repeatable pattern in Figure 6 is the seasonal variations of $\overline{E}_{pm}$ and $\overline{E}_{pv}$, with summer minima and winter maxima every year for McMurdo, despite the fact that $\overline{E}_{pm}$ and $\overline{E}_{pv}$ of individual segments could vary substantially from observation to observation. Such seasonal variations are, in general, similar to the previous lidar observations of stratospheric $\overline{E}_{pm}$ at Rothera (Yamashita et al., 2009) and Davis (Kaifler et al., 2015) in Antarctica. Nevertheless, the multiple years of high-quality lidar data at McMurdo provide the first time series of repeatable seasonal patterns of $\overline{E}_{pm}$ and $\overline{E}_{pv}$ in the Antarctic stratosphere. Similar analyses are done for $\overline{N^2}$, and the results are plotted in Figure 7. The altitude mean $\overline{N^2}$ also exhibits repeated seasonal patterns, which varies from minima (less than 4×10^{-4} s^{-2}) around October to maxima (over 5.5×10^{-4} s^{-2}) in winter. The peak-to-peak variation of $\overline{N^2}$ is ~40%, with the mean around 4.7×10^{-4} s^{-2}. Although the maxima for $\overline{E}_{pm}$ and $\overline{N^2}$ both occur around midwinter, the minimum $\overline{N^2}$ occurs around October, but the minimum $\overline{E}_{pm}$ occurs around late January and early
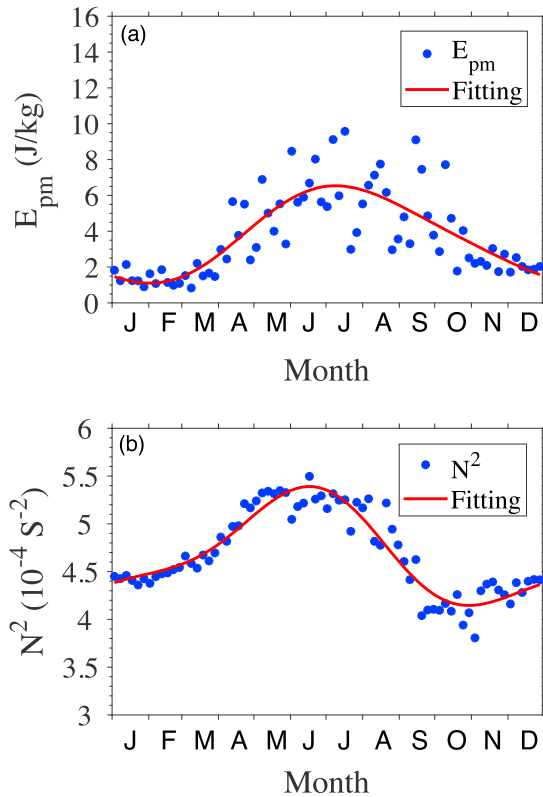
Figure 8. Five-year average annual cycles of $\overline{E}_{pm}$ and $\overline{N^2}$ binned every 5 days at McMurdo. The red lines are the harmonic fits given by equation (19).

February. Such differences indicate that even at polar latitudes, the seasonal change of $\overline{N^2}$ is unlikely the major cause of the observed seasonal variations of $\overline{E}_{pm}$ and $\overline{E}_{pv}$, although it may contribute.

To quantify the seasonal variations of $\overline{E}_{pm}$ and $\overline{N^2}$ and to compare with Yamashita et al. (2009), Figure 8 shows the 5-year average time series of $\overline{E}_{pm}$ and $\overline{N^2}$ with data binned every 5 days. Then we apply the harmonic fittings to the folded data and to the 5-year time series:

$$y = A_0 + A_{12} \cos\left[\frac{2\pi}{365}(x - \Phi_{12})\right] + A_6 \cos\left[\frac{2\pi}{365/2}(x - \Phi_6)\right], \quad (19)$$

where A_0 is the annual mean, A_{12} and A_6 are the amplitudes of annual and semiannual variations, and Φ_{12} and Φ_6 are the corresponding phases. Such harmonic fittings to multiple years of $\overline{E}_{pm}$ and $\overline{N^2}$ help mitigate the uneven sampling dictated by weather conditions. There are multiple ways to do the fitting for different purposes. To characterize the overall seasonal variations through 5 years, the harmonic fitting is applied to all the 5 years of data and yields the red curve shown in Figure 6a, which assumes constant amplitudes and continuous phases through these 5 years. The obtained fitting parameters are summarized in the first row of Table 4. The annual variation dominates over the semiannual variation. The annual variation peaks in the midwinter (July), while the semiannual variation peaks about 1 month earlier (see the first row of Table 4). The harmonic fitting to the $\overline{E}_{pm}$ data shown in Figure 8a gives results (see the second row in Table 4) nearly identical to the first fitting. Similar harmonic fittings are performed on $\overline{N^2}$ as indicated by the red lines in Figures 7a and 8b. The fitting parameters are summarized in the first two rows of Table 5.

To assess the interannual variability, the harmonic fitting given by equation (19) is applied to each individual year as illustrated in Figure 6b, and the fitting parameters are summarized in the third to seventh rows of Table 4. The annual variation amplitudes in 2015 and 2012 are larger than those in 2011, 2013, and 2014. It will be shown later that this difference is likely related to critical level filtering but not to variations in static stability. The semiannual variation phase in 2011 is nearly out of phase with that in other years. Overall, the 5 years of lidar data exhibit quite large year-to-year variability, which may also be related to the high variability of the timing of the vortex breakdown in November/December from year to year (e.g., Lübken et al., 2015). Similar harmonic fitting analyses are applied to $\overline{N^2}$ data in Figure 7b, and the fitting parameters are summarized in Table 5. The interannual variations of $\overline{N^2}$ are much smaller in both amplitude and phase when compared to $\overline{E}_{pm}$. The $\overline{N^2}$ fitting results for the annual and semiannual variations do not have large

Table 4
Fitting Parameters and Errors for $\overline{E}_{pm}$ in Figures 6 and 8

Case	A_0 (J/kg)	A_{12} (J/kg)	Φ_{12} (day)	A_6 (J/kg)	Φ_6 (day)
Figure 6a	3.89 ± 0.30	2.75 ± 0.40	200 ± 9	0.35 ± 0.43	166 ± 34
Figure 8a	3.78 ± 0.34	2.64 ± 0.48	202 ± 11	0.32 ± 0.48	161 ± 43
Figure 6b (2011)	3.92 ± 0.60	2.26 ± 0.80	210 ± 22	0.87 ± 0.88	88 ± 26
Figure 6b (2012)	4.26 ± 0.69	3.54 ± 1.00	204 ± 18	1.44 ± 1.01	180 ± 20
Figure 6b (2013)	3.23 ± 0.58	1.69 ± 0.79	191 ± 29	0.53 ± 0.83	143 ± 44
Figure 6b (2014)	3.51 ± 0.59	2.46 ± 0.85	216 ± 18	0.12 ± 0.80	226 ± 39
Figure 6b (2015)	4.35 ± 0.43	4.32 ± 0.57	187 ± 9	0.92 ± 0.57	186 ± 19

Table 5
Fitting Parameters and Errors for $\overline{N^2}$ in Figures 7 and 8

Case	A_0 (× 10^{-4} s^{-2})	A_{12} (× 10^{-4} s^{-2})	Φ_{12} (day)	A_6 (× 10^{-4} s^{-2})	Φ_6 (day)
Figure 5a	4.70 ± 0.02	0.55 ± 0.02	154 ± 3	0.17 ± 0.02	178 ± 4
Figure 6b	4.69 ± 0.03	0.56 ± 0.04	154 ± 5	0.17 ± 0.04	180 ± 8
Figure 5b (2011)	4.70 ± 0.05	0.61 ± 0.06	156 ± 7	0.28 ± 0.08	178 ± 7
Figure 5b (2012)	4.67 ± 0.04	0.49 ± 0.05	145 ± 8	0.20 ± 0.06	167 ± 8
Figure 5b (2013)	4.67 ± 0.04	0.50 ± 0.05	146 ± 8	0.16 ± 0.06	171 ± 12
Figure 5b (2014)	4.75 ± 0.03	0.59 ± 0.04	153 ± 5	0.15 ± 0.05	181 ± 10
Figure 5b (2015)	4.67 ± 0.02	0.57 ± 0.02	160 ± 3	0.09 ± 0.02	189 ± 9

changes over the 5 years. The annual component peaks at ~154 DOY, while the semiannual component maximizes at ~178 DOY.

The temperature data resolutions (2 hr by 1 km) used above are chosen to achieve sufficient SNRs for both winter and summer. If we consider only winter when the SNR is significantly higher (due to the low solar background), temperature data can be retrieved at 1 hr and 1 km resolutions. Indeed, we did such a test in Figure 6c. That is, when using resolutions of 1 hr and 1 km to derive winter temperatures, the obtained $\overline{E}_{pm}$ can be as large as 40 J/kg. For the original data processing, the integration window is 2 hr but the oversampled display resolution is 1 hr, so the minimum resolved temporal resolution of waves included in the original $\overline{E}_{pm}$ lies in between 2 and 4 hr. Using 1-hr time resolution enables us to include all waves with periods of 2 hr and longer. Figure 6c shows that including the full wave spectra from 2 to 4 hr substantially enhances (nearly doubles) $\overline{E}_{pm}$ at altitudes of 30–50 km. The absolute values of $\overline{E}_{pm}$ are comparable to lidar observations at both Rothera and Davis with similar seasonal variations (Alexander et al., 2011; Kaifler et al., 2015; Yamashita et al., 2009) but are larger than at the South Pole where $\overline{E}_{pm}$ is nearly constant throughout the year at a low value (~2.8 J/kg; Yamashita et al., 2009). Note that different wave spectra are included due to different data resolutions used in these studies. Gravity waves with periods of ~1–6 hr and vertical wavelengths of 2–30 km are included in the study of Yamashita et al. whereas Kaifler et al. put more emphasis on waves with periods longer than 2 hr and vertical wavelengths of ~4–20 km. In this study, we include waves with periods of ~2–11 hr and vertical wavelengths of ~2–30 km.
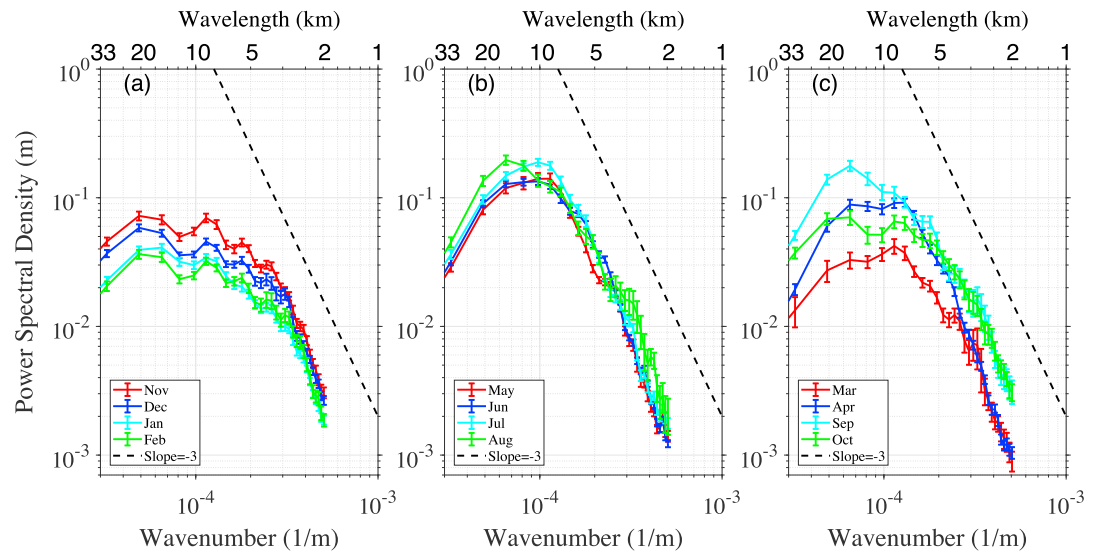
6. Monthly Mean Vertical Wave Number Spectra

In a previous study we investigated the seasonal-mean vertical wave number spectra and revealed the PSD of gravity waves with vertical wavelengths of 5–20 km increasing from summer minima to winter maxima at McMurdo (Zhao et al., 2017). Such seasonal variations of vertical wave number PSD are qualitatively consistent with the seasonal variations of $\overline{E}_{pm}$. Here we expand the study of Zhao et al. (2017) and compute monthly mean PSDs (see Figure 9).

Similar to Zhao et al. (2017), Lu et al. (2015), and Dewan and Grossbard (2000), the power spectral density of an individual vertical profile is derived as

$$\text{PSD}(m_k) = \frac{\left|\widehat{f}(m_k)\right|^2}{F_s \cdot N_z} \tag{20}$$

where m_k is the kth vertical wave number, $\widehat{f}(m_k)$ is the fast Fourier transform (FFT) value at m_k, $F_s = 1/\Delta z$ is the sampling rate (here Δz is the vertical interval of the data), and N_z is the FFT data size, that is, the total number of data points of the single vertical profile that is zero-padded and run through the FFT function. It is worth to note a dimensional analysis (Chen & Chu, 2017) that $\left|\widehat{f}(m_k)\right|^2$ represents power in FFT, and the power spectral density given in equation (20) is equivalent to energy. Under current data resolutions, there are no apparent white noise floors at the high wave number end of the spectra. Therefore, noise floors were not subtracted from the obtained spectra, similar to the practice by Gardner et al. (1989), Lu et al. (2015), and Zhao et al. (2017). We group the calculated PSDs into 12 months and average them within each month to obtain the monthly means. The average is weighted by observational time length, and the error bars are calculated

Figure 9. Five-year mean distributions of vertical wave number spectra for each month of the year. (left) Summer months (November through February), (middle) winter months (May through August), and (right) fall and spring months (March, April, September, and October).

as the standard errors (Zhao et al., 2017). A single vertical profile in our studies contains 21 original data points (30–50 km at 1-km interval), and it is zero-padded to 64 data points for FFT. For energy conservation in Fourier transform, $N_z = 64$ is used in equation (20) for this study, which is an improvement over the practice by Zhao et al. (2017) when $N_z = 21$ was used there so energy was not conserved. This difference in choosing N_z explains why the vertical wave number PSDs in Figure 8b of Zhao et al. (2017) are somewhat higher than those in the current Figure 9. Nevertheless, the differences in the absolute values of PSDs do not affect the determination of characteristic vertical wave numbers and the slopes of PSDs.

The variations of PSDs throughout a year can be clearly identified. Maximum PSD for vertical wavelengths between 5 and 20 km is evident during the winter months, which corresponds to on average longer vertical wavelengths in winter. The PSD for the shortest vertical wavelengths remains nearly identical throughout the year. The characteristic vertical wave number (m^*), that is, the transition vertical wave number between the positive and negative slopes in the PSD spectra, is ~1×10^{-4} m^{-1} from March to July and about 6.5×10^{-5} m^{-1} in August and September, whereas there is no distinguishable m^* from October to February.

To quantify the slope changes through a year, we perform linear fittings to the vertical wave number spectra in the range of 2–10 km. The resulting slopes and associated errors are summarized in Table 6. The slopes exhibit distinct seasonal signatures—steep slopes around -3 from April to July, but much shallower around -2 from October to February.

Compared to the winter values, summer PSD values between 5 and 20 km are significantly smaller. As for the fall (March and April) and spring (September and October) seasons, it is interesting that March and September exhibit PSDs nearly identical to the summer and winter PSDs, respectively, while April and October show the transitions from summer to winter and from winter to summer, respectively. Such PSD variations in the m-spectra are consistent with the seasonal variations of $\overline{E}_{pm}$ and $\overline{E}_{pv}$ inferred from Figures 6 and 8a. The characteristic vertical wavelengths increase from a shorter wavelength in March (representing summer) to a longer wavelength in September (representing winter) and then return to shorter wavelengths in October and summer. Such spectral behaviors are also consistent with the seasonal results in Zhao et al. (2017).

7. Correlations of $\overline{E}_{pm}$ With Polar Vortex, Wind Rotation, and Wind Speeds

Whiteway et al. (1997) and Duck et al. (1998) have found that the amount of gravity wave energy in the upper stratosphere at Eureka in the Arctic is related to the position of the stratospheric polar vortex. They showed that gravity wave activity was a maximum within the westerly jet at the edge of the vortex, a minimum inside

Table 6
Slopes of Monthly Mean Vertical Wave Number Spectra in Figure 9

Range	Jan	Feb	Mar	Apr	May	Jun	Jul	Aug	Sep	Oct	Nov	Dec
2–10 km	−1.76 ± 0.24	−1.63 ± 0.30	−2.46 ± 0.27	−3.17 ± 0.28	−3.14 ± 0.19	−3.19 ± 0.26	−3.20 ± 0.18	−2.64 ± 0.23	−2.35 ± 0.21	−2.00 ± 0.26	−1.90 ± 0.29	−1.71 ± 0.29

the vortex near its center, and intermediate outside the vortex (Whiteway et al., 1997). Baumgaertner and McDonald (2007) have found from the CHAMP/GPS observations that $\overline{E}_{pm}$ at 23–27 km shows gravity wave enhancement within ±10° from the vortex edge. For the gravity wave potential energy density from 30 to 45 km at Rothera, Antarctica, Yamashita et al. (2009) have found that all the large $\overline{E}_{pm}$ events were observed between +5 and −10° from the vortex edge. To examine the polar vortex effects, we calculate the McMurdo position relative to the polar vortex edge at an altitude of 32 km using global wind and temperature data from the Modern Era Retrospective Analysis for Research and Applications version 2 (MERRA-2; Bosilovich et al., 2015). The Antarctic vortex edge is defined as follows. The "Q diagnostic" measures the relative contribution of strain and rotation in the flow (Malvern, 1969); Q is negative in regions where rotation is dominant and positive where there is strong shear. Starting at the center of cyclonic wind systems, the Q diagnostic is integrated around concentric stream function (ψ) contours (aligned parallel to the rotational wind) and nodes in Q are vortex edge candidates. The vortex edge is defined as the candidate ψ contour where line-integrated wind speed maximizes. See Harvey et al. (2002) for a more extensive description of the algorithm. According to the results shown in Figure 10a, there are small $\overline{E}_{pm}$ values (<4 J/kg) for all possible positions of McMurdo relative to the polar vortex edge; however, the major high-level gravity wave activity ($\overline{E}_{pm}$>10 J/kg) occurs when McMurdo is about +3 to −23° relative to the vortex edge. In particular, the very large $\overline{E}_{pm}$ values (>15 J/kg) occur when McMurdo lies well inside the polar vortex (about 8–23° poleward from the vortex edge). While this result appears to contradict some previous observational results mentioned above, what we may be seeing is simply a wintertime maximum in GW activity. In other words, without another lidar site that is coincident with the vortex edge in midwinter, it is not clear whether even higher gravity wave activity occurs at the edge during the May–August timeframe. Figure 10b illustrates the number of lidar observations during the presence of polar vortex. The distribution starts in March (9 points), peaks in May through July, and ends in November (20 points). The Antarctic vortex is not present from December to February (see also Figure 13e). Figure 10b also illustrates the distance of McMurdo station from the vortex edge, which clearly shows that on average McMurdo stays deep inside the vortex during midwinter.

Yamashita et al. (2009) suggested that critical level filtering of gravity waves by the background winds, orographic wave generation in the lower troposphere, and in situ generation of gravity waves by large wind shear at the edge of the polar vortex could have contributed to the observed seasonal variations of $\overline{E}_{pm}$ at Rothera. Following these hints, wind data from ECMWF at McMurdo are used here to inspect the correlations between $\overline{E}_{pm}$ and several potential factors. In Figures 11a–11c, we plot the 5 years of lidar-observed $\overline{E}_{pm}$ along with wind rotation angles from 11 to 30 km, absolute wind speeds at 3 km and at 30 km, respectively, given by the ECMWF reanalysis data. Despite some fluctuations in the data, it is obvious from these three figures that $\overline{E}_{pm}$ are anticorrelated with the wind rotation angles and positively correlated with the wind speeds at both 3 and 30 km. The correlation coefficients of monthly mean $\overline{E}_{pm}$ with monthly mean wind rotation angles, near-surface winds at 3 km, and stratospheric winds at 30 km (see Figure 11) are −0.62, +0.87, and +0.80, respectively. All these correlations have 95% confidence levels. In the following we show that these correlations are significant.

Wind rotation angles from lower altitudes to the observed region are taken as a proxy for critical level filtering effects. As pointed out by Yamashita et al. (2009), large wind rotation angles usually indicate that wind profiles cross the zero wind lines, providing critical levels for orographic gravity waves with nearly zero phase speeds and other low phase speed waves. Thus, the large wind rotation angles during summer will largely filter out gravity waves that are produced by winds blowing over the trans-Antarctic mountains, islands near the Antarctic continent, or Antarctic Peninsula, or by winds blowing down the Antarctic Ice Sheet. In contrast, the small wind rotation angles in winter indicate that orographic gravity waves and other gravity waves propagating against the tropospheric mean flow (i.e., predominantly westward waves) have much larger probabilities of penetrating through the troposphere and reaching the stratosphere. To quantify this point, we group $\overline{E}_{pm}$ observations with their corresponding wind rotation angles at McMurdo. PDFs are plotted for wind rotation angles larger than 180° and less than 100° in Figure 12a, while the corresponding cumulative distribution functions (CDF) are plotted in Figure 12b. Almost all large $\overline{E}_{pm}$ occur during the periods with small wind rotation angles, that is, in winter. As shown in Figure 11, the wind rotation angles in 2012 and 2015 winters are consistently small throughout the winter, in contrast to the other three winters having much more
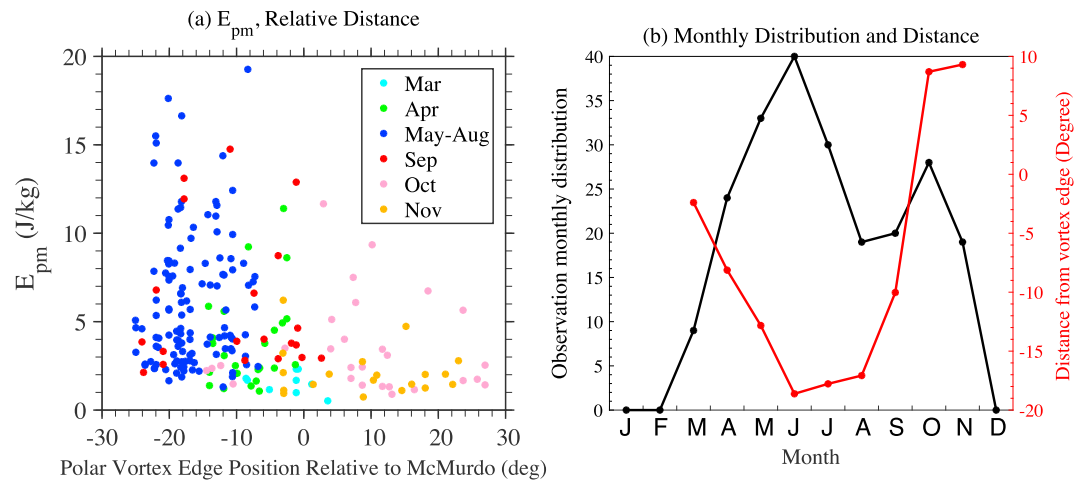
Figure 10. (a) $\overline{E}_{pm}$ versus polar vortex edge position relative to McMurdo color coded by season. Zero degree means that McMurdo is at the polar vortex edge, negative degrees mean that McMurdo is inside the vortex, and positive degrees mean that McMurdo is outside the vortex. (b) Monthly distribution of the number of lidar observations (black line) during the presence of polar vortex in Antarctica and the monthly mean distance between McMurdo and the vortex edge (red line), as given above. The Antarctic vortex is not present from December to February.
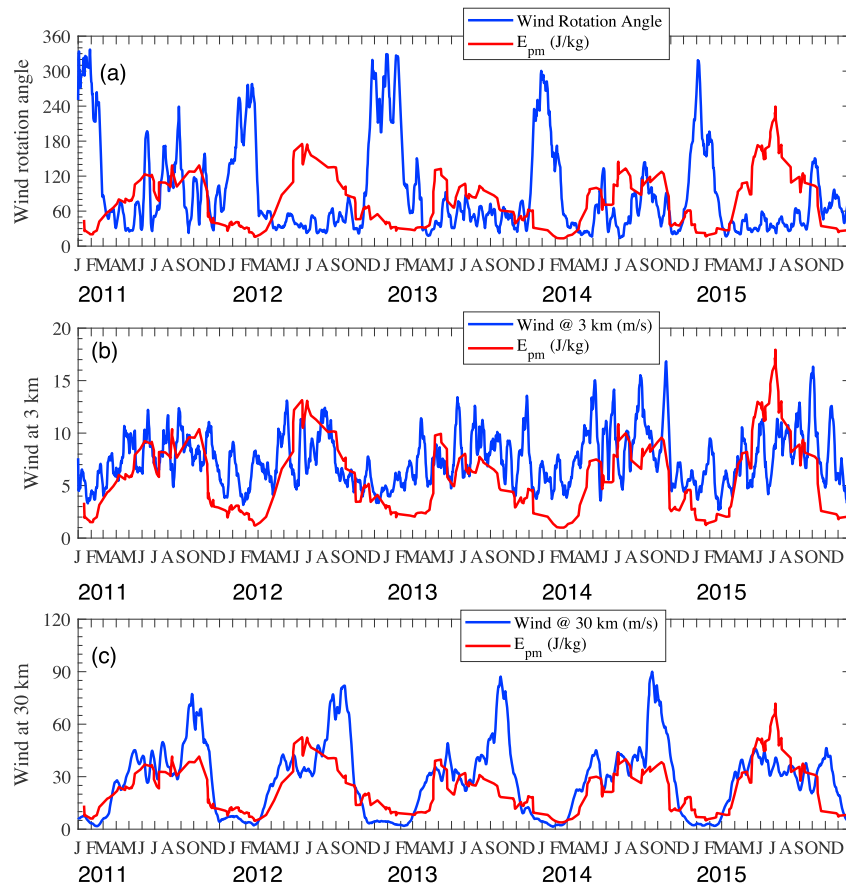
Figure 11. Time series of $\overline{E}_{pm}$ versus (a) wind rotation angle between 11 and 30 km, (b) surface wind at 3 km, and (c) stratospheric wind at 30 km given by ECMWF at McMurdo. A 14-day running mean is applied to smooth the ECMWF data (wind rotation angles, 3- and 30-km wind speeds) with a 1-day step, while a seven-point running mean is used to smooth the lidar-measured $\overline{E}_{pm}$ with a one-point step. $\overline{E}_{pm}$ is multiplied by 20, 1.5, and 6 in (a) to (c), respectively.
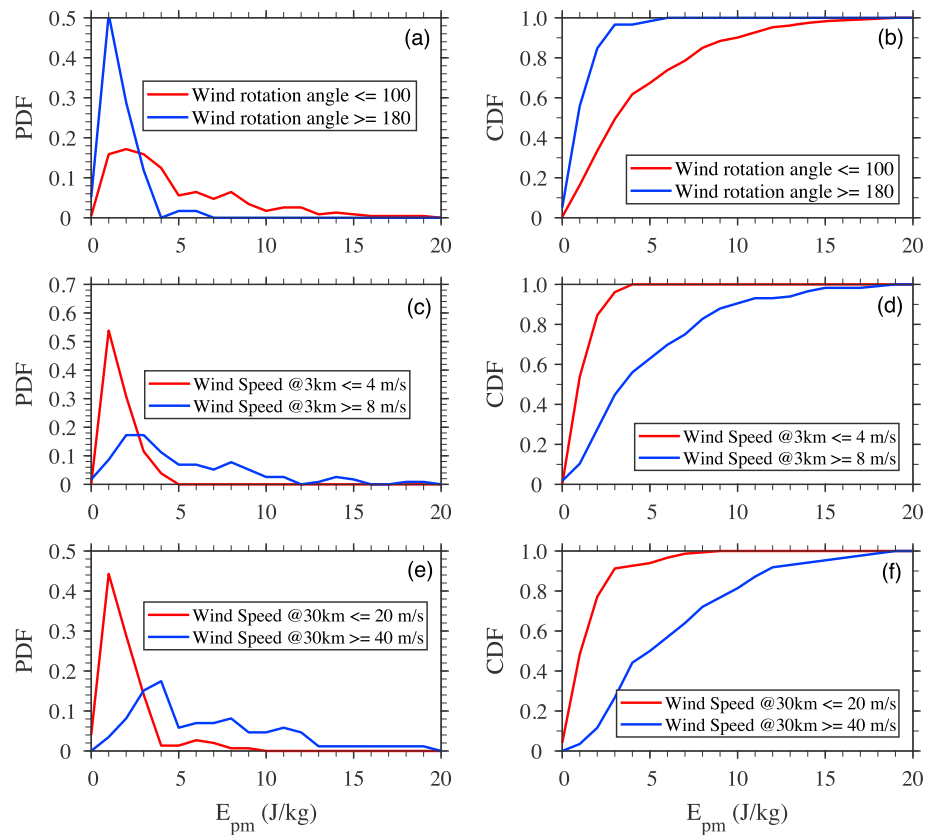
Figure 12. (a) Probability density functions (PDFs) and (b) cumulative distribution functions (CDFs) of $\overline{E}_{pm}$ under different wind rotation angles (i.e., larger than 180° or smaller than 100°). (c) PDF and (d) CDF of $\overline{E}_{pm}$ under different surface wind conditions (i.e., larger than 8 m/s or smaller than 4 m/s). (e) PDF and (f) CDF of $\overline{E}_{pm}$ under different stratospheric wind conditions (i.e., larger than 40 m/s or smaller than 20 m/s). ECMWF wind rotation angles and 3- and 30-km wind speeds at McMurdo are smoothed with a 7-day running mean with a 1-day step. The lidar-measured raw $\overline{E}_{pm}$ data are not smoothed.

variable wind rotations. Such differences in wind rotation angles are consistent with the observations that $\overline{E}_{pm}$ in 2012 and 2015 winters are higher than those in other three winters.

Near-surface wind speed at McMurdo is taken as a proxy of the forcing strength for generation of orographic gravity waves. Faster surface winds in winter than in summer favor the generation of more orographic gravity waves in winter. Hence, the wave sources in winter are expected to be stronger than those in summer. We group the $\overline{E}_{pm}$ observations with corresponding near-surface winds (at 3 km) and show the corresponding PDF and CDF in Figures 12c and 12d. $\overline{E}_{pm}$ amounts to ~5 J/kg in the slower wind case. Large $\overline{E}_{pm}$ events occur only in the faster wind case, and the positive correlation between $\overline{E}_{pm}$ and the near-surface wind speed is strong. When choosing only the data during small wind rotation angles (<100°) and redrawing Figures 12c and 12d, the positive correlation is even stronger as $\overline{E}_{pm}$ goes up to only ~3 J/kg in the slower wind case and all larger $\overline{E}_{pm}$ occur in the faster wind case (not shown). This result of strong positive correlation is different from that of Yoshiki and Sato (2000) who found a weak correlation between lower stratospheric $\overline{E}_{pm}$ and the surface wind speed at two Antarctic stations: Syowa (69.0°S, 39.6°E) and Casey (66.3°S, 110.5°E). This difference may be caused by differences in the alignment of topography and surface wind direction, as suggested by Watanabe et al. (2006). Westward downslope (katabatic) winds on the East Antarctic Ice Sheet can excite orographic gravity waves over Syowa and Casey Stations. However, the mean wind in the lower stratosphere is eastward in Antarctic winter and spring, so there is a critical level (zero wind line) for the orographic waves (Yoshiki & Sato, 2000). Consequently, such orographic gravity waves will not be observed at higher altitudes, losing the correlation between stratospheric gravity wave energy and the surface wind. Contrarily, at McMurdo, most large $\overline{E}_{pm}$ events occurring from May to September are most likely caused by eastward downslope (katabatic) winds blowing down the steep slopes of the East Antarctic Ice Sheet by
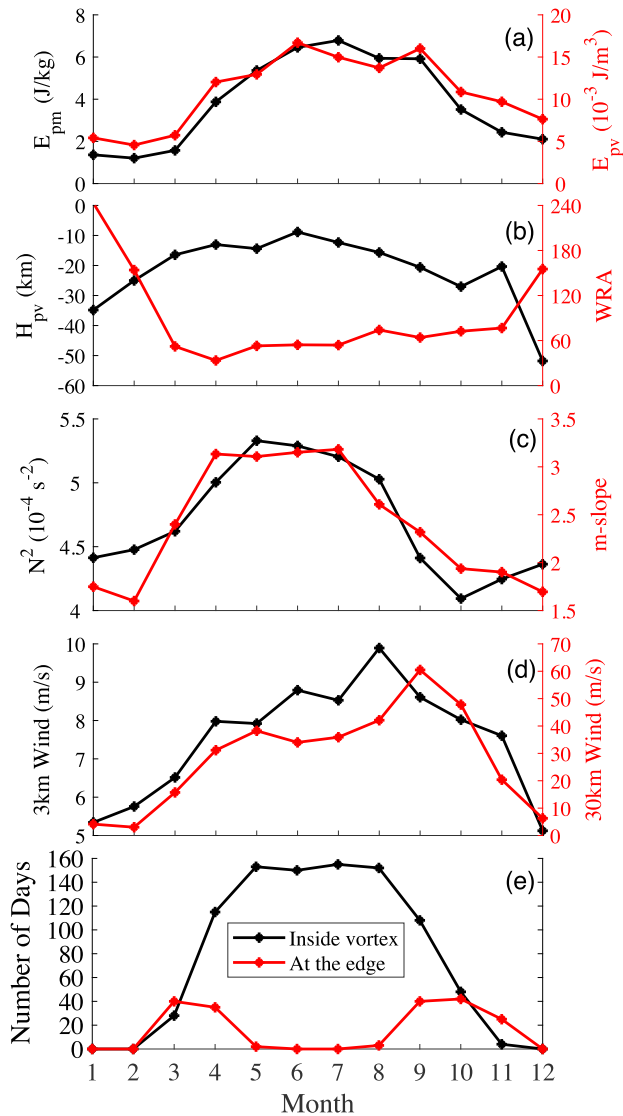
Figure 13. Monthly mean gravity wave parameters and atmospheric conditions at McMurdo. (a) Altitude mean $\overline{E}_{pm}$ (black) and $\overline{E}_{pv}$ (red), (b) scale height H_{pv} (black) and wind rotation angle (WRA, red) from 11 to 30 km, (c) monthly mean $\overline{N^2}$ (black) and slopes (red)of monthly mean vertical wave number spectra in the vertical wavelength range of 2–10 km, (d) ECMWF total wind speeds at 3-km (black) and 30-km (red) altitudes near McMurdo location, and (e) the total number of days during 5 years of 2011–2015 when McMurdo is inside the polar vortex ($<-5°$, black) and at the vortex edge (within ±5°, red).

the west coast of Ross Sea (Watanabe et al., 2006). Such orographic gravity waves can propagate upward through the winter eastward winds into the stratosphere, as the critical level filtering is minimal, leading to the strong positive correlation observed at McMurdo. The McMurdo results along with Syowa and Casey results support the suggestion by Watanabe et al. (2006) for roles played by the alignment of topography relative to the surface wind.

Stratospheric wind speed at 30 km is taken as a proxy of forcing strength for in situ generation of nonorographic gravity waves. Strong winter stratospheric winds, once forming unbalanced flow, can generate gravity waves via geostrophic adjustment (e.g., Fritts & Luo, 1992; Nicolls et al., 2010; Sato & Yoshiki, 2008; Vadas & Fritts, 2001; Zhu & Holton, 1987). Stratospheric wind speed at 30 km is also a proxy for the Doppler shifting effect. Whiteway et al. (1997) and Duck et al. (2001) have proposed that high stratospheric winds induce Doppler shift, shifting waves toward longer vertical wavelengths. The winter maxima of $\overline{E}_{pm}$ observed at McMurdo are likely related to the increase of vertical wavelength toward winter (Figure 4 in Zhao et al., 2017), allowing larger wave amplitudes before reaching saturation. This point can be explained by the linear saturation theory—longer λ_z waves can grow to larger wave amplitudes (N^2/m^3) before saturating (Lindzen, 1981; Whiteway et al., 1997), leading to higher $\overline{E}_{pm}$ in winter than in summer. We group $\overline{E}_{pm}$ with their corresponding stratospheric winds at 30 km. PDF and CDF are shown in Figures 12e and 12f. It is obvious that higher $\overline{E}_{pm}$ correspond to faster stratospheric winds at 30 km. Such strong positive correlation is also true for winds at 40 and 50 km (not shown).

We now discuss the possible causes of the observed seasonal variations of $\overline{E}_{pm}$, λ_z, and vertical wave number PSD, combining the results from this study with the Part I study by Zhao et al. (2017). Several monthly mean wave parameters are plotted in Figure 13, complementing the monthly mean vertical and horizontal wavelengths, ground-relative and intrinsic periods, vertical phase speed, and horizontal and vertical group velocities given by Figures 4 and 9 in Zhao et al. (2017). A major conjecture from our observational results is that the large summer-winter asymmetry observed in $\overline{E}_{pm}$ is mainly caused by the critical level filtering of gravity waves by the prevailing wind system (see Figure 4 in Becker, 2012). In our study this mechanism is represented by the wind rotation angle (Figure 13b). During summer, most gravity waves are filtered out by the prevailing wind system except the waves with significant eastward phase speeds that become important near the meso-

pause only. In contrast, under eastward prevailing winds during wintertime, the majority of gravity waves originating from the lower atmosphere (with westward phase speeds, near-zero phase speeds, and low eastward phase speeds) survive into the observed altitude range (30–50 km), growing to large amplitudes. Larger wave amplitudes and more surviving waves in winter lead to the higher values of $\overline{E}_{pm}$ than in summer. Because the strong critical level filtering in summer has significantly attenuated gravity wave amplitudes before these waves reach 30–50 km, the summer waves in the 30–50-km range experiences less severe dissipation than the large amplitude waves in winter, explaining the H_{pv} seasonal variations in Figure 13b. An interesting remark is that the wind rotation angles in 2012 and 2015 winters (Figure 11a) appear to be smaller and less variable than those in the winters of 2011, 2013, and 2014. This relation is consistent with the observational results that winter $\overline{E}_{pm}$ in 2012 and 2015 are generally larger than in the other three winters. Hence, critical level filtering likely plays a key role in the observed interannual variations of $\overline{E}_{pm}$.

Another conjecture from the observational results is that the variations of $\overline{E}_{pm}$ from March to October, when the critical level filtering is minimal, are mainly determined by the near-surface winds that are associated with the generation of orographic gravity waves and by the stratospheric winds that are associated with in situ generation of nonorographic gravity waves (Figure 13d) and with Doppler shifting of the vertical wave-lengths of gravity waves. The major sources of gravity waves in winter over McMurdo are likely orographic gravity waves produced by downslope (katabatic) winds that blow down from the East Antarctic Ice Sheet onto the Ross Sea (Becker & Vadas, 2018; Watanabe et al., 2006). The positive correlation between $\overline{E}_{pm}$ and the near-surface wind at 3 km is strong and statistically significant and so is the positive correlation between $\overline{E}_{pm}$ and the stratospheric wind (see also Figure 12). In addition, high stratospheric winds can Doppler shift waves toward longer vertical wavelengths as proposed by Whiteway et al. (1997) and Duck et al. (2001), which allows larger wave amplitudes in winter before reaching saturation as explained above. The increase of the atmospheric stability $\overline{N^2}$ from summer to winter (Figure 13c) also allows larger amplitudes of gravity waves during wintertime, but it plays only a secondary role in this context. Moreover, wave dissipation due to the strong stratospheric winds can produce intermittent horizontal body forces that generate secondary gravity waves in the stratosphere and lower mesosphere (Becker & Vadas, 2018; Vadas et al., 2003, 2018). This process may also change the wave spectra, leading to altered wave saturation. As the dominant waves over McMurdo propagate obliquely with small elevation angles ~1.1° (Zhao et al., 2017), gravity waves in the McMurdo stratosphere could have originated from orographic wave sources and in situ wave sources (e.g., polar vortex edge) that are far away from McMurdo, explaining the observations of large $\overline{E}_{pm}$ despite McMurdo often being deep inside the polar vortex.

8. Conclusions

A statistical study has been conducted to characterize E_{pm}, E_{pv}, N^2, and vertical wave number spectra in the stratosphere using the Rayleigh temperatures from Fe Boltzmann lidar observations from 2011 to 2015 at McMurdo, Antarctica. This study represents the first lidar observations of repeated seasonal patterns of stratospheric gravity wave potential energy densities and atmospheric static stability N^2 in Antarctica. E_{pm}, E_{pv}, and N^2 profiles in the altitude range of 30–50 km are derived from 5 years of lidar-measured temperature perturbations and gradients. The scale heights H_{pv} show that wave dissipation in winter is much more severe than in summer. Altitude mean $\overline{E}_{pm}$ and $\overline{E}_{pv}$ vary significantly from observation to observation, but they exhibit repeated seasonal patterns with winter maxima and summer minima. The winter maxima in 2012 and 2015 are higher than in other years, exhibiting interannual variations. $\overline{E}_{pm}$ and $\overline{E}_{pv}$ obey lognormal distributions and possess narrowly clustered small values in summer, widely spread large values in winter, and intermediate values in spring and fall. Altitude mean $\overline{N^2}$ also exhibits seasonal variations with maxima in midwinter but minima around October. The peak-to-peak variation of $\overline{N^2}$ is ~40%, with the mean around 4.7×10^{-4} s^{-2}. The statistical distributions of $\overline{N^2}$ are different from lognormal but nearly bimodal. The monthly mean vertical wave number power spectral density for vertical wavelengths of 5–20 km increases from summer to winter and decreases back via transition months April and October, respectively. The seasonal asymmetry in the spectra corresponds to the observed statistically longer vertical wavelengths of gravity waves in winter.

Using MERRA-2 data to determine the polar vortex edge position, we find that the largest $\overline{E}_{pm}$ occur in midwinter when McMurdo is deep inside the polar vortex. We need another lidar site that is situated at the vortex edge in midwinter to determine whether gravity wave activity peaks at the Antarctic vortex edge as is the case in the Arctic (e.g., Whiteway et al., 1997). Using ECMWF data to represent the wind fields over McMurdo, we find that large gravity wave $\overline{E}_{pm}$ events occur when the wind rotation angles (representing critical level filtering) are small and when both the near-surface wind speeds at 3 km (representing the forcing strength of orographic gravity waves) and the stratospheric wind speeds at 30 km (representing the forcing strength of nonorographic gravity waves and Doppler shifting effect) are large. The monthly mean $\overline{E}_{pm}$ are anticorrelated with ECMWF monthly mean wind rotation angles while positively correlated with near-surface winds and stratospheric winds with correlations of −0.62, +0.87, and +0.80, respectively, at 95% confidence level. These correlations are strong and statistically significant.

We conclude from these results that the large summer-winter asymmetry observed in $\overline{E}_{pm}$ is mainly caused by the critical level filtering of gravity waves by the prevailing wind system that induces dissipation of most gravity waves in summer around the tropopause and in the lower stratosphere. The variations of $\overline{E}_{pm}$ from March to October, when the critical level filtering is minimal, are mainly determined by the near-surface winds that generate orographic gravity waves and by the stratospheric winds that generate nonorographic gravity waves and Doppler shift gravity waves to longer vertical wavelengths. The major sources of gravity waves in winter over McMurdo are likely orographic gravity waves produced by downslope (katabatic) winds that travel down the surface slopes of the East Antarctic Ice Sheet. Polar vortex, possessing high-speed stratospheric winds, has two major effects on gravity waves: an important source of nonorographic wave generation and Doppler shift effects that allow large gravity wave amplitudes before reaching wave saturation. The highest PSD in the λ_z range of 5–20 km, the longest vertical wavelengths, and the highest $\overline{E}_{pm}$ in winter are all consistent with each other. Therefore, $\overline{E}_{pm}$ seasonal variations are determined by the combined seasonal changes in critical level filtering from the troposphere to the stratosphere, orographic wave generation near the surface, in situ wave generation in the stratosphere, and modulation of wave saturation by the stratospheric mean winds during wintertime.

Quantitative determination of contributions from various aforementioned factors requires gravity wave modeling and ray tracing analysis that are beyond the scope of this work, but it could be the subject of future work. Other remaining questions, for example, include (1) What do the lognormal distributions of vertical wavelength, ground-relative period, vertical phase speed, and $\overline{E}_{pm}$ imply about wave sources and dissipation? (2) What are the sources of dominant waves in the stratosphere, especially during summer? (3) What causes the interannual variations of $\overline{E}_{pm}$? It is worth pointing out that the first part of our statistical study by Zhao et al. (2017) focused on dominant gravity waves only, but the potential energy density calculation in this second part includes contributions from all gravity waves whose parameters fall within the spectral range determined by the lidar data resolutions. Therefore, this work complements Zhao et al. (2017) in terms of both wave activity strength and broader wave spectra. In the future, the combination of wave characteristics, wave energies, and wave number and frequency spectra will help identify sources of persistent gravity waves in the MLT and contribute to studies of wave coupling from the lower to the middle and upper atmosphere.

References

Alexander, M. J., Geller, M., McLandress, C., Polavarapu, S., Preusse, P., Sassi, F., et al. (2010). Recent developments in gravity-wave effects in climate models and the global distribution of gravity-wave momentum flux from observations and models. *Quarterly Journal of the Royal Meteorological Society*, *136*, 1103–1124. https://doi.org/10.1002/qj.637

Alexander, M. J., Gille, J., Cavanaugh, C., Coffey, M., Craig, C., Eden, T., et al. (2008). Global estimates of gravity wave momentum flux from High Resolution Dynamics Limb Sounder observations. *Journal of Geophysical Research*, *113*, D15S18. https://doi.org/10.1029/2007JD008807

Alexander, S. P., Klekociuk, A. R., & Murphy, D. J. (2011). Rayleigh lidar observations of gravity wave activity in the winter upper stratosphere and lower mesosphere above Davis, Antarctica (69°S, 78°E). *Journal of Geophysical Research*, *116*, D13109. https://doi.org/10.1029/2010JD015164

Baumgaertner, A. J. G., & McDonald, A. J. (2007). A gravity wave climatology for Antarctica compiled from Challenging Minisatellite Payload/Global Positioning System (CHAMP/GPS) radio occultations. *Journal of Geophysical Research*, *112*, D05103. https://doi.org/10.1029/2006JD007504

Becker, E. (2012). Dynamical control of the middle atmosphere. *Space Science Reviews*, *168*(1-4), 283–314. https://doi.org/10.1007/s11214-011-9841-5

Becker, E., & Vadas, S. L. (2018). Secondary gravity waves in the winter mesosphere: Results from a high-resolution global circulation model. *Journal of Geophysical Research: Atmospheres*, *123*, 2605–2627. https://doi.org/10.1002/2017JD027460

Bosilovich, M., Akella, S., Coy, L., Cullather, R., Draper, C., Gelaro, R., et al. (2015). MERRA-2: Initial evaluation of the climate. In *NASA Technical Report Series on Global Modeling and Data Assimilation* (Tech. Rep. NASA/TM-2015-104606, Vol. 43, 136 pp.). NASA.

Chen, C., & Chu, X. (2017). Two-dimensional Morlet wavelet transform and its application to wave recognition methodology of automatically extracting two-dimensional wave packets from lidar observations in Antarctica. *Journal of Atmospheric and Solar: Terrestrial Physics*, *162*, 28–47. https://doi.org/10.1016/j.jastp.2016.10.016

Chen, C., Chu, X., McDonald, A. J., Vadas, S. L., Yu, Z., Fong, W., & Lu, X. (2013). Inertia-gravity waves in Antarctica: A case study using simultaneous lidar and radar measurements at McMurdo/Scott Base (77.8°S, 166.7°E). *Journal of Geophysical Research: Atmospheres*, *118*, 2794–2808. https://doi.org/10.1002/jgrd.50318

Chen, C., Chu, X., Zhao, J., Roberts, B. R., Yu, Z., Fong, W., et al. (2016). Lidar observations of persistent gravity waves with periods of 3–10 h in the Antarctic middle and upper atmosphere at McMurdo (77.83°S, 166.67°E). *Journal of Geophysical Research: Space Physics*, *121*, 1483–1502. https://doi.org/10.1002/2015JA022127

Chu, X., Huang, W., Fong, W., Yu, Z., Wang, Z., Smith, J. A., & Gardner, C. S. (2011). First lidar observations of polar mesospheric clouds and Fe temperatures at McMurdo (77.8°S, 166.7°E), Antarctica. *Geophysical Research Letters*, *38*, L16810. https://doi.org/10.1029/2011GL048373

Chu, X., Pan, W., Papen, G. C., Gardner, C. S., & Gelbwachs, J. A. (2002). Fe Boltzmann temperature lidar: Design, error analysis, and initial results at the North and South Poles. *Applied Optics*, *41*(21), 4400–4410. https://doi.org/10.1364/AO.41.004400

Chu, X., & Papen, G. C. (2005). Resonance fluorescence lidar for measurements of the middle and upper atmosphere. In T. Fujii & T. Fukuchi (Eds.), *Laser Remote Sensing* (pp. 179–432). Boca Raton, FL: CRC Press, Taylor & Francis Group.

Chu, X., & Yu, Z. (2017). Formation mechanisms of neutral Fe layers in the thermosphere at Antarctica studied with a thermosphere-ionosphere Fe/Fe$^+$ (TIFe) model. *Journal of Geophysical Research: Space Physics*, *122*, 6812–6848. https://doi.org/10.1002/2016JA023773

Chu, X., Z. Yu, W. Fong, C. Chen, J. Zhao, I. F. Barry et al. (2016). From Antarctica lidar discoveries to OASIS exploration, Proceedings of the 27th International Laser Radar Conference, EPJ Web of Conferences, 119, 12001, New York. https://doi.org/10.1051/epjconf/201611912001

Chu, X., Yu, Z., Gardner, C. S., Chen, C., & Fong, W. (2011). Lidar observations of neutral Fe layers and fast gravity waves in the thermosphere (110–155 km) at McMurdo (77.8°S, 166.7°E), Antarctica. *Geophysical Research Letters*, *38*, L23807. https://doi.org/10.1029/2011GL050016

Dewan, E. M., & Grossbard, N. (2000). Power spectral artifacts in published balloon data and implications regarding saturated gravity wave theories. *Journal of Geophysical Research*, *105*(D4), 4667–4683. https://doi.org/10.1029/1999JD901108

Duck, T. J., Whiteway, J. A., & Carswell, A. I. (1998). Lidar observations of gravity wave activity and arctic stratospheric vortex core warming. *Geophysical Research Letters*, *25*(15), 2813–2816. https://doi.org/10.1029/98GL02113

Duck, T. J., Whiteway, J. A., & Carswell, A. I. (2001). The gravity wave–Arctic stratospheric vortex interaction. *Journal of the Atmospheric Sciences*, *58*, 3581–3596. https://doi.org/10.1175/1520-0469(2001)058<3581:TGWASV>2.0.CO;2

Fong, W., Chu, X., Lu, X., Chen, C., Fuller-Rowell, T. J., Codrescu, M., & Richmond, A. D. (2015). Lidar and CTIPe model studies of the fast amplitude growth with altitude of the diurnal temperature "tides" in the Antarctic winter lower thermosphere and dependence on geomagnetic activity. *Geophysical Research Letters*, *42*, 697–704. https://doi.org/10.1002/2014GL062784

Fong, W., Lu, X., Chu, X., Fuller-Rowell, T. J., Yu, Z., Roberts, B. R., et al. (2014). Winter temperature tides from 30 to 110 km at McMurdo (77.8°S, 166.7°E), Antarctica: Lidar observations and comparisons with WAM. *Journal of Geophysical Research: Atmospheres*, *119*, 2846–2863. https://doi.org/10.1002/2013JD020784

Fritts, D. C., & Alexander, M. J. (2003). Gravity wave dynamics and effects in the middle atmosphere. *Reviews of Geophysics*, *41*(1), 1003. https://doi.org/10.1029/2001RG000106

Fritts, D. C., & Luo, Z. (1992). Gravity wave excitation by geostrophic adjustment of the jet stream. Part 1: Two-dimensional forcing. *Journal of the Atmospheric Sciences*, *49*(8), 681–697. https://doi.org/10.1175/1520-0469(1992)049<0681:GWEBGA>2.0.CO;2

Garcia, R. R., López-Puertas, M., Funke, B., Marsh, D. R., Kinnison, D. E., Smith, A. K., & González-Galindo, F. (2014). On the distribution of CO_2 and CO in the mesosphere and lower thermosphere. *Journal of Geophysical Research: Atmospheres*, *119*, 5700–5718. https://doi.org/10.1002/2013JD021208

Gardner, C. S., Senft, D. C., Beatty, T. J., Bills, R. E., & Hostetler, C. A. (1989). Rayleigh and sodium lidar techniques for measuring middle atmospheric density, temperature and wind perturbations and their spectra. In C. H. Liu & B. Edwards (Eds.), *World ionosphere/thermosphere study handbook* (Vol. 2, pp. 148–187). Urbana, Ill: Int. Congr. of Sci. Unions.

Geller, M. A., Alexander, M. J., Love, P. T., Bacmeister, J., Ern, M., Hertzog, A., et al. (2013). A comparison between gravity wave momentum fluxes in observations and climate models. *Journal of Climate*, *26*(17), 6383–6405. https://doi.org/10.1175/JCLI-D-12-00545.1

Godin, O. A., & Zabotin, N. A. (2016). Resonance vibrations of the Ross Ice Shelf and observations of persistent atmospheric waves. *Journal of Geophysical Research: Space Physics*, *121*, 10,157–10,171. https://doi.org/10.1002/2016JA023226

Harvey, V. L., Pierce, R. B., Fairlie, T. D., & Hitchman, M. H. (2002). A climatology of stratospheric polar vortices and anticyclones. *Journal of Geophysical Research*, *107*(D20), 4442. https://doi.org/10.1029/2001JD001471

Hauchecorne, A., Chanin, M. L., Keckhut, P., & Nedeljkovic, D. (1992). Lidar monitoring of the temperature in the middle and lower atmosphere. *Applied Physics B: Lasers and Optics*, *55*(1), 29–34. https://doi.org/10.1007/BF00348609

Hertzog, A., Alexander, M. J., & Plougonven, R. (2012). On the intermittency of gravity wave momentum flux in the stratosphere. *Journal of the Atmospheric Sciences*, *69*(11), 3433–3448. https://doi.org/10.1175/JAS-D-12-09.1

Hines, C. O. (1960). Internal atmospheric gravity waves at ionospheric heights. *Canadian Journal of Physics*, *38*(11), 1441–1481. https://doi.org/10.1139/p60-150

Hines, C. O. (1974). *The upper atmosphere in motion* (pp. 13–344). Washington, DC: American Geophysical Union. https://doi.org/10.1029/GM018p0014

Hitchman, M. H., Gille, J. C., Rodgers, C. D., & Brasseur, G. (1989). The separated polar winter stratopause: A gravity wave driven climatological feature. *Journal of the Atmospheric Sciences*, *46*, 410–422. https://doi.org/10.1175/1520-0469(1989)046<0410:TSPWSA>2.0.CO;2

Hoffmann, P., Becker, E., Singer, W., & Placke, M. (2010). Seasonal variation of mesospheric waves at northern middle and high latitudes. *Journal of Atmospheric and Solar-Terrestrial Physics*, *72*(14-15), 1068–1079. https://doi.org/10.1016/j.jastp.2010.07.002

Holton, J. R. (1982). The role of gravity wave induced drag and diffusion in the momentum budget of the mesosphere. *Journal of the Atmospheric Sciences*, *39*, 791–799. https://doi.org/10.1175/1520-0469(1982)039<0791:TROGWI>2.0.CO;2

Holton, J. R. (1983). The influence of gravity wave breaking on the general circulation of the middle atmosphere. *Journal of the Atmospheric Sciences*, *40*, 2497–2507. https://doi.org/10.1175/1520-0469(1983)040<2497:TIOGWB>2.0.CO;2

Kaifler, B., Lübken, F.-J., Höffner, J., Morris, R. J., & Viehl, T. P. (2015). Lidar observations of gravity wave activity in the middle atmosphere over Davis (69°S, 78°E), Antarctica. *Journal of Geophysical Research: Atmospheres*, *120*, 4506–4521. https://doi.org/10.1002/2014JD022879

Kim, Y.-J., Eckermann, S. D., & Chun, H.-Y. (2003). An overview of the past, present and future of gravity wave drag parameterization for numerical climate and weather prediction models. *Atmosphere-Ocean*, *41*, 65–98. https://doi.org/10.3137/ao.410105

Lindzen, R. S. (1981). Turbulence and stress owing to gravity wave and tidal breakdown. *Journal of Geophysical Research*, *86*(C10), 9707–9714. https://doi.org/10.1029/JC086iC10p09707

Lu, X., Chu, X., Chen, C., Nguyen, V., & Smith, A. K. (2017). First observations of short-period eastward propagating planetary waves from the stratosphere to the lower thermosphere (110 km) in winter Antarctica. *Geophysical Research Letters*, *44*, 10,744–10,753. https://doi.org/10.1002/2017GL075641

Lu, X., Chu, X., Fong, W., Chen, C., Yu, Z., Roberts, B. R., & McDonald, A. J. (2015). Vertical evolution of potential energy density and vertical wave number spectrum of Antarctic gravity waves from 35 to 105 km at McMurdo (77.8°S, 166.7°E). *Journal of Geophysical Research: Atmospheres*, *120*, 2719–2737. https://doi.org/10.1002/2014JD022751

Lu, X., Chu, X., Fuller-Rowell, T., Chang, L., Fong, W., & Yu, Z. (2013). Eastward propagating planetary waves with periods of 1–5 days in the winter Antarctic stratosphere as revealed by MERRA and lidar. *Journal of Geophysical Research: Atmospheres*, *118*, 9565–9578. https://doi.org/10.1002/jgrd.50717

Lübken, F.-J., Höffner, J., Viehl, T. P., Becker, E., Latteck, R., Kaifler, B., et al. (2015). Winter/summer transition in the Antarctic mesopause region. *Journal of Geophysical Research: Atmospheres*, *120*, 12,394–12,409. https://doi.org/10.1002/2015JD023928

Malvern, L. E. (1969). *Introduction to the mechanics of a continuous medium* (pp. 120–135). Englewood Cliffs, NJ: Prentice-Hall.

McLandress, C., Ward, W. E., Fomichev, V. I., Semeniuk, K., Beagley, S. R., McFarlane, N. A., & Shepherd, T. G. (2006). Large-scale dynamics of the mesosphere and lower thermosphere: An analysis using the extended Canadian Middle Atmosphere Model. *Journal of Geophysical Research*, *111*, D17111. https://doi.org/10.1029/2005JD006776

Murphy, D. J., Alexander, S. P., Klekociuk, A. R., Love, P. T., & Vincent, R. A. (2014). Radiosonde observations of gravity waves in the lower stratosphere over Davis, Antarctica. *Journal of Geophysical Research: Atmospheres*, *119*, 11,973–11,996. https://doi.org/10.1002/2014JD022448

Mzé, N., Hauchecorne, A., Keckhut, P., & Thétis, M. (2014). Vertical distribution of gravity wave potential energy from long-term Rayleigh lidardata at a northern middle-latitude site. *Journal of Geophysical Research: Atmospheres*, *119*, 12,069–12,083. https://doi.org/10.1002/2014JD022035

Nicolls, M. J., Varney, R. H., Vadas, S. L., Stamus, P. A., Heinselman, C. J., Cosgrove, R. B., & Kelley, M. C. (2010). Influence of an inertia-gravity wave on mesospheric dynamics: A case study with the Poker Flat Incoherent Scatter Radar. *Journal of Geophysical Research*, *115*, D00N02. https://doi.org/10.1029/2010JD014042

Picone, J. M., Hedin, A. E., Drob, D. P., & Aikin, A. C. (2002). NRLMSISE-00 empirical model of the atmosphere: Statistical comparisons and scientific issues. *Journal of Geophysical Research*, *107*(A12), 1468. https://doi.org/10.1029/2002JA009430

Plougonven, R., & Zhang, F. (2014). Internal gravity waves from atmospheric jets and fronts. *Reviews of Geophysics*, *52*, 33–76. https://doi.org/10.1002/2012RG000419

Richter, J. H., Sassi, F., & Garcia, R. R. (2010). Toward a physically based gravity wave source parameterization in a general circulation model. *Journal of the Atmospheric Sciences*, *67*(1), 136–156. https://doi.org/10.1175/2009JAS3112.1

Sato, K., & Yoshiki, M. (2008). Gravity wave generation around the polar vortex in the stratosphere revealed by 3 hourly radiosonde observations at Syowa Station. *Journal of the Atmospheric Sciences*, *65*(12), 3719–3735. https://doi.org/10.1175/2008JAS2539.1

Shibuya, R., Sato, K., Tsutsumi, M., Sato, T., Tomikawa, Y., Nishimura, K., & Kohma, M. (2017). Quasi-12 h inertia–gravity waves in the lower mesosphere observed by the PANSY radar at Syowa Station (39.6° E, 69.0° S). *Atmospheric Chemistry and Physics*, *17*(10), 6455–6476. https://doi.org/10.5194/acp-17-6455-2017

Vadas, S. L., & Fritts, D. C. (2001). Gravity wave radiation and mean responses to local body forces in the atmosphere. *Journal of the Atmospheric Sciences*, *58*(16), 2249–2279. https://doi.org/10.1175/1520-0469(2001)058<2249:GWRAMR>2.0.CO;2

Vadas, S. L., Fritts, D. C., & Alexander, M. J. (2003). Mechanism for the generation of secondary waves in wave breaking regions. *Journal of the Atmospheric Sciences*, *60*, 194–214. https://doi.org/10.1175/1520-0469(2003)060<0194:MFTGOS>2.0.CO;2

Vadas, S. L., Zhao, J., Chu, X., & Becker, E. (2018). The excitation of secondary gravity waves from body forces: Theory and observation. *Journal of Geophysical Research: Atmospheres*. https://doi.org/10.1029/2017JD027970

Wang, Z., Chu, X., Huang, W., Fong, W., Smith, J. A., & Roberts, B. (2012). Refurbishment and upgrade of Fe Boltzmann/Rayleigh temperature lidar at Boulder for McMurdo lidar campaign in Antarctica, Proceeding of the 26th International Laser Radar Conference, 207–210, Porto Heli, Greece, 25–29 June 2012.

Watanabe, S., Sato, K., & Takahashi, M. (2006). A general circulation model study of the orographic gravity waves over Antarctica excited by katabatic winds. *Journal of Geophysical Research*, *111*, D18104. https://doi.org/10.1029/2005JD006851

Whiteway, J. A., & Carswell, A. I. (1995). Lidar observations of gravity wave activity in the upper stratosphere over Toronto. *Journal of Geophysical Research*, *100*(D7), 14,113–14,124. https://doi.org/10.1029/95JD00511

Whiteway, J. A., Duck, T. J., Donovan, D. P., Bird, J. C., Pal, S. R., & Carswell, A. I. (1997). Measurements of gravity wave activity within and around the Arctic stratospheric vortex. *Geophysical Research Letters*, *24*(11), 1387–1390. https://doi.org/10.1029/97GL01322

Wilson, R., Chanin, M. L., & Hauchecorne, A. (1991). Gravity waves in the middle atmosphere observed by Rayleigh lidar: 1. Case studies. *Journal of Geophysical Research*, *96*(D3), 5153–5167. https://doi.org/10.1029/90JD02231

Yamashita, C., Chu, X., Liu, H.-L., Espy, P. J., Nott, G. J., & Huang, W. (2009). Stratospheric gravity wave characteristics and seasonal variations observed by lidar at the South Pole and Rothera, Antarctica. *Journal of Geophysical Research*, *114*, D12101. https://doi.org/10.1029/2008JD011472

Yasuda, Y., Sato, K., & Sugimoto, N. (2015). A theoretical study on the spontaneous radiation of inertia-gravity waves using the renormalization group method. Part I: Derivation of the renormalization group equations. *Journal of the Atmospheric Sciences*, *72*(3), 957–983. https://doi.org/10.1175/JAS-D-13-0370.1

Yoshiki, M., & Sato, K. (2000). A statistical study of gravity waves in the polar regions based on operational radiosonde data. *Journal of Geophysical Research*, *105*(D14), 17,995–18,011. https://doi.org/10.1029/2000JD900204

Yu, Z., Chu, X., Huang, W., Fong, W., & Roberts, B. R. (2012). Diurnal variations of the Fe layer in the mesosphere and lower thermosphere: Four season variability and solar effects on the layer bottomside at McMurdo (77.8°S, 166.7°E), Antarctica. *Journal of Geophysical Research*, *117*, D22303. https://doi.org/10.1029/2012JD018079

Zhao, J., Chu, X., Chen, C., Lu, X., Fong, W., Yu, Z., et al. (2017). Lidar observations of stratospheric gravity waves from 2011 to 2015 at McMurdo (77.84° S, 166.69° E), Antarctica: 1. Vertical wavelengths, periods, and frequency and vertical wavenumber spectra. *Journal of Geophysical Research: Atmospheres*, *122*, 5041–5062. https://doi.org/10.1002/2016JD026368

Zhu, X., & Holton, J. R. (1987). Mean fields induced by local gravity-wave forcing in the middle atmosphere. *Journal of the Atmospheric Sciences*, *44*(3), 620–630. https://doi.org/10.1175/1520-0469(1987)044<0620:MFIBLG>2.0.CO;2